GLC_FCS10: a global 10-m land-cover dataset with a fine classification system from Sentinel-1 and Sentinel-2 time-series data in Google Earth Engine

Xiao Zhang [1,2], Liangyun Liu [1,2,3*], Tingting Zhao [1,4], Wenhan Zhang [1,2,3], Linlin Guan[1,2], Ming Bai [1,5], and Xidong Chen [6]

1 International Research Center of Big Data for Sustainable Development Goals, Beijing, 100094, China.

2 Key Laboratory of Digital earth Science, Aerospace information Research institute, Chinese Academy of Sciences, Beijing, 100094, China.

3 School of electronic, electrical and communication engineering, University of Chinese Academy of Sciences, Beijing, 100049, China.

4 School of Geography and Ocean Science, Nanjing University, Nanjing, Jiangsu 210023, China.

5 College of Geomatics, Xi'an University of Science and Technology, Xi'an 710054, China.

6 Future Urbanity & Sustainable environment (FUSE) Lab, the University of Hong Kong, Hong Kong, 999007, China.

Corresponding author: Liangyun Liu (liuly@radi.ac.cn)

Abstract

The continuous development of remote sensing techniques provides ample opportunities for high-resolution land-cover mapping. Although global 10-m land-cover products have made considerable progress over past few years, their simple classification system makes it difficult to meet the needs of diverse applications. In this work, we propose a hierarchical land-cover mapping framework to produce a novel global 10-m land-cover dataset with a fine classification system (called GLC_FCS10) using Sentinel-1 and Sentinel-2 time-series observations from 2023. First, the globally distributed training samples are hierarchically obtained from multisource prior products after applying a series of refinements. Then, a combination of hierarchical land-cover mapping, local adaptive modeling, and multisource features is used to produce land-cover maps for each 5 × 5 geographical tile. Next, using 56121 globally distributed validation samples and a third-party validation dataset (LCMAP_Val), the GLC_FCS10 is assessed. The GLC_FCS10 achieves an overall accuracy of 83.16% and a kappa coefficient of 0.789 globally and an overall accuracy of 85.09% in the United States. Meanwhile, comparisons with five released 10- or 30-m land-cover products also demonstrate that GLC_FCS10 has higher accuracy and captures more diverse land-cover information than three of the released global 10-m land-cover products. In summary, the novel GLC_FCS10 land-cover maps can provide important support for high-resolution land-cover related research and applications. The GLC_FCS10 can be freely access via https://doi.org/10.5281/zenodo.14729665 (Liu and Zhang, 2025).

1. Introduction

Land-cover information is a vital component of global climate change research and plays an important role in climate change mitigation, biodiversity protection, and global food security (Foley et al., 2005; Liu et al., 2021). With advancements in satellite techniques and computational and storage capabilities, global land-cover mapping has made substantial progresses. A series of global land-cover products, ranging from 1-km to 10-m resolutions, has been continuously released (Giri et al., 2013; Liu et al., 2021). Recently, Wang et al. (2023) reviewed the characteristics of global land-cover products and found that land-cover mapping has evolved from coarse to high spatial resolution. Currently, four global 10-m land-cover products are available, including FROM_GLC10 (Gong et al., 2019), ESRI LC (Karra et al., 2021), European Space Agency (ESA) WorldCover (Buchhorn et al., 2020), and Dynamic World (Brown et al., 2022). However, all of these products use a simple classification system, which limits their applicability for specific and fine applications (Zhang et al., 2021). Meanwhile, the work of Zhao et al. (2023) explained that FROM_GLC10, ESRI LC, and ESA WorldCover have relatively low consistency and accuracy. Thus, developing an accurate global 10-m land-cover dataset with a fine classification system is still necessary.

The diversity of land-cover types depends on the training samples, and there are two options to generate a globally distributed training pool—visual interpretation and automated derivation from prior products (Zhang and Roy, 2017; Zhang et al., 2021). Visual interpretation means that experts or volunteers interpreted the land-cover information through high-resolution imagery, Google Earth Streetview photos, or other auxiliary datasets. For example, the training samples in FROM_GLC10 were derived from expert interpretations and contained approximately 93,000 sites worldwide (Gong et al., 2013), and the ESA WorldCover used 20 trained experts to collect approximately 141,000 training locations from the Geo-Wiki engagement platform (Buchhorn et al., 2020). Obviously, training sites from the "visual interpretation" option can ensure high quality (Ban et al., 2015), however, the problems of cost and time are not to be ignored. The diversity of the land-cover classification system also relies on the experts' prior knowledges. The "automated derivation from prior products" option generates the training sites from prior land-cover datasets after taking some refinements or validations (Radoux et al., 2014; Zhang et al., 2021; Zhang et al., 2024c). For example, the training areas in the GLC_FCS30 were collected from a combination of time-series MCD43A4 surface reflectance data and CCI_LC land-cover products after using some spatiotemporal purification methods, and these automatically derived training samples supported high-accuracy land-cover mapping with overall accuracy of 82.5% (Zhang et al., 2021). The automated option enables more efficient collection of globally confident training samples; however, the classification errors of prior land-cover products were also easier to transfer into the derived training samples (Zhang and Roy, 2017). Therefore, it is critical to avoid transferring error into the training samples.

Another great challenge in global land-cover mapping lies in the choice of suitable methodologies. Currently, the vast majority of global land-cover mapping ignores the complexity and sparsity of various land-cover types and completes a mapping project with a single classification model (Friedl et al., 2010; Gong et al., 2013), which leads to considerable uncertainties in sparse (e.g., impervious surfaces) or complex (e.g., wetlands and shrubland) land-cover types (Karra et al., 2021; Zhang et al., 2021; Zhao et al., 2023). Several measures were taken to improve the performance of large-area land-cover mapping, such as: local adaptive modeling (Defourny et al., 2018; Li et al., 2023; Zhang and Roy, 2017; Zhang et al., 2021), hierarchical land-cover mapping (Chen et al., 2015; Sulla-Menashe et al., 2019), or integration of multisource datasets (Yu et al., 2014; Zhang et al., 2020).

Local adaptive modeling first split study area into many local areas and further trained corresponding classification models within each local region to improve the ability to capture regional characteristics. Zhang and Roy (2017) found that local adaptive modeling had higher accuracy than single global land-cover modeling, however, it also needs enough training samples to support regional modeling. Hierarchical land-cover mapping divides the

land surface into various land-cover layers, and some complicated land-cover layers may need to be treated independently. Taking wetlands as an example, most global land-cover products perform poorly on wetlands because of their varied spectral characteristics and complicated spatiotemporal features (Buchhorn et al., 2020; Gong et al., 2019; Zhang et al., 2021). The GlobeLand30 achieved 74.87% accuracy with wetlands because this land-cover type was treated independently (Chen et al., 2015). Hierarchical land-cover mapping gives more attention to complicated land-cover types by importing more prior knowledge (Chen et al., 2015) or adding sufficient high-confidence training samples (Zhang et al., 2023b). many previous works have demonstrated the integration of multisource datasets, such as optical imagery (Landsat and Sentinel-2) and Sentinel-1 single-aperture radar (SAR) data to improve the identification of impervious surfaces (Zhang et al., 2020), wetlands (Zhang et al., 2023b), forests (Tang et al., 2023), or croplands (Blickensdörfer et al., 2022; Sun et al., 2024). Therefore, multisource data effectively enhances land-cover mapping.

The free access to Sentinel imagery and to the powerful cloud computation platform provide ample opportunity for global land-cover mapping at 10 m. In this work, we developed an accurate and novel global 10-m land-cover product (called GLC_FCS10) containing 30 fine land-cover types from Sentinel-1 and Sentinel-2 time-series imagery. To achieve this goal, we propose: 1) a hierarchical land-cover mapping framework to decrease the uncertainties of impervious surfaces and wetlands; 2) to combine the prior multisource land-cover datasets and the metric centroid to automatically generate a globally distributed and high-confidence 10-m training pool; 3) to integrate time-series Sentinel-2 optical and Sentinel-1 SAR data for producing the new GLC_FCS10 on the GEE platform; 4) to comprehensively compare the developed GLC_FCS10 with several previous products.

2. Datasets

2.1 Satellite imagery

All available Sentinel-2 surface reflectance imagery for 2023 were atmospherically corrected using the Sen2Cor tool, and the corrected images were then stored on the GEE platform. This imagery contains 12 spectral bands from visible to shortwave infrared and a revisiting period of 5 days (Berger et al., 2012; Radeloff et al., 2024). In this work, the four 10-m visible and near-infrared bands and six 20-m red edges and shortwave infrared bands were used, while the two 60-m bands of aerosols and water vapor were excluded to minimize atmospheric effects. The six 20-m reflectance imagery bands were resampled to 10-m using the bilinear resampling method (Berger et al., 2012). Any poor-quality pixels, including clouds and shadows, were masked using the quality control band (QA60) and the cloud probability product.

Sentinel-1 has a dual-polarization (VV and VH) C-band SAR instrument with a revisiting period of 6 days after launching of Sentinel-1B (Torres et al., 2012). In this work, all Sentinel-1 imagery for 2023 were obtained through the GEE platform, which have been preprocessed through radiometric calibration, thermal noise removal, and terrain correction, and further resampled their resolution of 5 m × 20 m into 10 m × 10 m using Sentinel-1 Toolbox when archived on the GEE platform.

Some previous works have demonstrated that topographical data can provide auxiliary and useful information in land-cover mapping (Zhang et al., 2023b), currently, global 10 m digital elevation model (DEM) is not yet available. In this work, we used the 30-m ASTER GDEM, which has low vertical error of 0.7 m (Tachikawa et al., 2011), to obtained the elevation, slope, and aspect after bilinear resampling to 10 m × 10 m.

2.2 Prior land-cover products

2.2.1 Impervious surface products

Impervious surfaces are characterized by sparse spatial distribution and complicated spectral and spatial heterogeneities; thus, it should be treated independently Its training samples are generated from five previous

products: 1) The Global 30-m Impervious Surface Dynamic (GISD30) dataset, developed with the combination of spectral generalization and sample migration during 1985-2020 with the interval of 5-years, achieves a fulfilling accuracy of 90.1% (Zhang et al., 2022). 2) The Global Impervious Surface Area (GISA 2.0) dataset, produced by considering the inconsistency among four existing products, is an annual time-series impervious surface maps during 1985-2018 with the F1-score of 0.935 (Huang et al., 2022). 3) The 10 m impervious surface layer in ESA WorldCover dataset was generated by the supervision classification from time-series Sentinel-1 and Sentinel-2 imagery (Zanaga et al., 2021). It was demonstrated to achieve the great performance with producer's accuracy of 82.99% (Zhao et al., 2023). 4) The impervious surface layer in ESRI Land Cover is developed from time-series Sentinel-2 imagery and the deep-learning (Karra et al., 2021), and achieve high producer's accuracy of 88.42% (Zhao et al., 2023) .5) Global urban boundary dataset (GUB) is generated by the combination of cellular-automata and morphological approach, and shows a good agreement with the results from human interpretation (Li et al., 2020).

Table 1. The characteristics of prior land-cover products.

Category	Dataset name	Resolution	Year	Coverage	Reference
Impervious surface	GISD30	30	1985–2020	Global	Zhang et al. (2022)
	GISA 2.0	30	1985–2019	Global	Huang et al. (2022)
	Imp-ESA_LC	10	2021	Global	Zanaga et al. (2021)
	Imp-ESRI_LC	10	2023	Global	Karra et al. (2021)
	GUB	-	2020	Global	Li et al. (2020)
Wetland	GWL_FCS30D	30	2000–2022	Global	Zhang et al. (2024b)
	National Wetland Inventory	30	2019	United States	Wilen and Bates (1995)
	Global Mangrove Watch	30	1996–2020	Global	Bunting et al. (2022)
	Global tidal flat	30	2000–2022	Global	Zhang et al. (2023a)
	Global tidal marsh dataset	10	2020	Global	Worthington et al. (2024)
Land-cover	GLC_FCS30D	30	1985–2022	Global	Zhang et al. (2024c)
	Global oil palm dataset	30	1990–2021	Global	Descals et al. (2024)
	Global plantation map	30	1982–2020	Global	Du et al. (2022)

2.2.2 Wetland products

Because almost all global land-cover products have large uncertainties in wetlands identification (Zhang et al., 2023b), wetlands should also be treated as independent land-cover type. The wetland training samples were also derived from three existing wetland thematic products, including: 1) the GWL_FCS30D is an annual global wetland products containing 8 wetland subcategories (5 inland and 3 coastal wetland subcategories), and achieves an overall accuracy of 86.95 ± 0.44% (Zhang et al., 2024b). 2) The NWI (National Wetland Inventory) is national wetland thematic products covering the whole United States and containing 8 wetland subcategories (Wilen and Bates, 1995). 3) The GMW (Global Mangrove Watch) and global tidal marsh products provide the spatial patterns of mangrove and salt marsh with the overall accuracy of 87.4% and 85% (Bunting et al., 2022; Worthington et al., 2024).

2.2.3 GLC_FCS30D land-cover dynamic products

Except for wetlands and impervious surfaces, training samples for the remaining non-wetland natural land-cover types are generated from the GLC_FCS30D dataset. It was developed from the combination of a continuous change detection algorithm with an adaptive updating strategy and had 80.88% (±0.27%) accuracy covering the period of 1985–2022 with 35 fine land-cover subcategories. The dataset has high temporal stability in the European Union and United States (Zhang et al., 2024c). In this work, we leverage this dynamic product to generate confident training samples for non-wetland natural land covers, as described in the Section 3.1.

2.2.4 Tree-cover cropland datasets

It is noteworthy that the tree-cover cropland was only mapped in certain regions rather than globally in the GLC_FCS30D (Zhang et al., 2021; Zhang et al., 2024c); thus, global oil palm and plantation datasets are also used to identify tree-cover cropland. The global oil palm dataset is a time-series covering 1990–2020 and exceeds 91% accuracy for industrial plantations and 71% accuracy for smallholders (Descals et al., 2024). A global plantation map was generated by combining some prior global plantation products and the LandTrendr method, and has an F1 score of 86.83% with ±5 years tolerance (Du et al., 2022).

3. Methodology

To achieve high quality with detailed categorizations in global 10-m land-cover mapping, a hierarchical land-cover mapping methodology has been proposed. It leverages prior land-cover products and time-series satellite observations, and gives more attention to impervious surfaces and wetlands by importing more prior knowledge and adding sufficient high-confidence training samples. Notably, the reasons why we separated impervious surfaces and wetlands from other land cover types include: 1) impervious surfaces are structurally different from natural land covers (Huang et al., 2022; Zhang et al., 2022); 2) wetlands are a highly zonal land-cover type (concentrating in low-lying areas) with extremely complex spectra and heterogeneities due to changes in phenology and water-levels (Mao et al., 2020; Zhang et al., 2023b); 3) many previous studies have demonstrated that many existing global land-cover products suffered poor performance on these complicated land-cover types (Zhao et al., 2023). Figure 1 presents a flowchart of the proposed method, which involves four procedures: generating hierarchical and globally distributed training samples from prior products, compositing multisource and multitemporal training features from time-series Sentinel 1&2 imagery, hierarchical land-cover mapping using local adaptive classifications, and accuracy assessment and cross-comparisons.
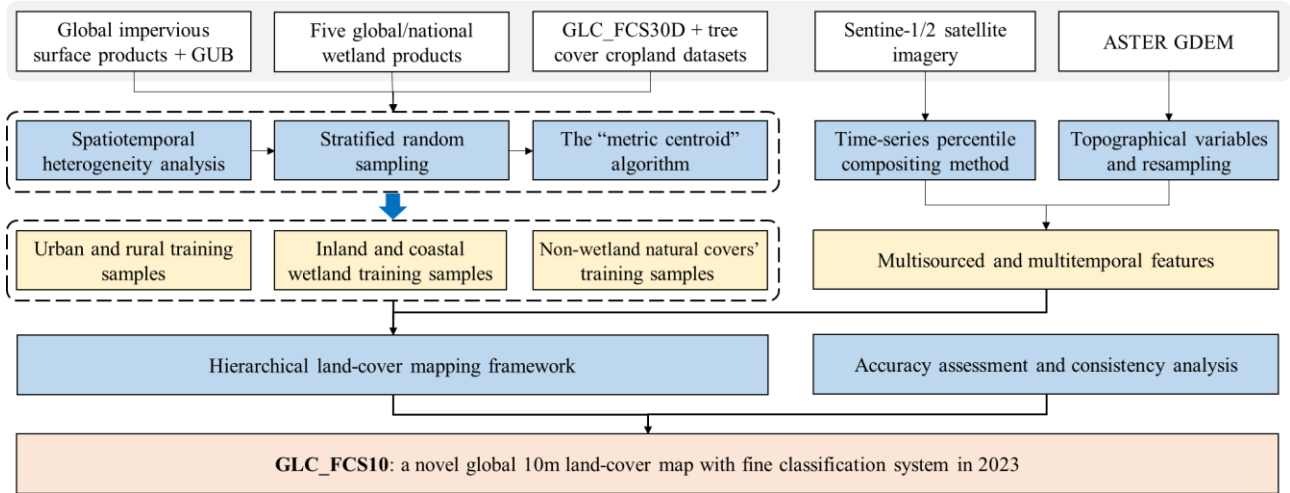
Figure 1. The flowchart of the proposed method for hierarchical land-cover mapping.

3.1 The description of the classification system

In this work, we develop a novel global 10-m land-cover dataset with a fine classification system (FCS). Table 2 presents the main characteristics of this FCS and its correspondence with the basic classification system. It contains 30 fine land-cover types and emphasizes the forest- and wetland-related subcategories, which are further subdivided into 10 and 7 subcategories, respectively. The diversity of this fine classification system results from importing the GWL_FCS30D (Zhang et al., 2024b) and GLC_FCS30D (Zhang et al., 2024c) products. It should be noted that the detailed descriptions about each fine land-cover type have been supplemented at the Table S1.

177 **Table 2**. The characteristics of the fine classification system in the GLC_FCS10.

Basic classification system	Detailed validation system	Fine classification system
Cropland	Rainfed cropland	Herbaceous rainfed cropland
		Tree or shrub covered rainfed cropland (orchard, oil palm…)
	Irrigated cropland	Irrigated cropland
Forest	Evergreen broadleaved forest	Closed evergreen broadleaved forest
		Open evergreen broadleaved forest
	Deciduous broadleaved forest	Closed deciduous broadleaved forest
		Open deciduous broadleaved forest
	Evergreen needleleaved forest	Closed evergreen needleleaved forest
		Open evergreen needleleaved forest
	Deciduous needleleaved forest	Closed deciduous needleleaved forest
		Open deciduous needleleaved forest
	Mixed-leaf forest	Closed mixed-leaf forest
		Open mixed-leaf forest
Shrubland	Shrubland	Evergreen shrubland
		Deciduous shrubland
Grassland	Grassland	Grassland
Tundra	Tundra	Lichens and mosses
Wetland	Wetland	Swamp
		Marsh
		Lake/river flat
		Saline
		Mangrove forest
		Salt marsh
		Tidal flat
Impervious surfaces	Impervious surfaces	Urban impervious surfaces
		Rural impervious surfaces
Bare areas	Sparse vegetation	Sparse vegetation
	Bare areas	Bare areas
Water	Water	Water
Permanent ice and snow	Permanent ice and snow	Permanent ice and snow

3.2 Generating hierarchical training samples

179   To ensure quality in global 10-m land-cover mapping, land surfaces are hierarchically divided into impervious
180 surface, wetland, and non-wetland natural land-cover types. Their corresponding training samples also need to be
181 generated independently. Because training sample quality greatly affects land-cover mapping performance (Foody
182 and Arora, 2010; Zhang and Roy, 2017), generating confident and globally distributed training samples is a
183 prerequisite for generating the GLC_FCS10.

3.2.1 Training areas of impervious surfaces

185   Regarding the training samples of impervious surfaces, we combine four prior global 10-m or 30-m impervious
186 surface products (GISA 2.0, GISD30, Imp-ESA_LC, and Imp-ESRI_LC) and one urban boundary dataset (GUB) to
187 automatically generate the training samples. Specifically, because the previous studies have demonstrated high-
188 accuracies of three impervious surface products (Huang et al., 2022; Zanaga et al., 2021; Zhang et al., 2022)and high
189 producer's accuracy of Imp-ESRI_LC (Zhao et al., 2023), the areas marked as impervious surfaces by all four
190 products (GISD30-2020, GISA2.0-2019, Imp-ESA_LC-2021, and Imp-ESRI_LC-2023) are selected as candidate
191 areas for generating the training samples (*TrainCanArea_imp*) in Eq. (1).

$$TrainCanArea_{imp} = GISD30 \cap \text{GISA2.0} \cap (\text{Imp-ESA}_{LC}) \cap (\text{Imp-ESRI\_LC}) \qquad (1)$$

192 Afterward, we further consider the uneven distribution of rural and urban impervious surfaces as well as their spectral

193 variability. If random sampling is used to obtain training samples from the *TrainCanArea_imp*, rural impervious
194 surfaces are underrepresented due to their sparse distribution, thus, the GUB urban boundary dataset for 2020 is
195 further used to divide the *TrainCanArea_imp* into urban (*TrainCanArea_urban*) and rural areas
196 (*TrainCanArea_rural*).
197   Beyond the confident impervious surface areas, it is equally important to identify high-quality natural land-cover
198 types (Zhang et al., 2024a). To avoid confusion between natural land-cover types and impervious surfaces, the
199 maximum impervious surface boundary (*MaxBound_imp*) is also generated. The training samples for natural land-
200 cover types should be located outside of the *MaxBound_imp*, i.e., some inner-city areas, easily misclassified or
201 confused with impervious surfaces, will be excluded because Imp-ESRI_LC exhibits extensive patches of the
202 impervious surface and lacks spatial details (Wang et al., 2024; Xu et al., 2024b). To determine *MaxBound_imp*, the
203 union of the four products is applied as:

$$MaxBound_{imp} = GISD30 \cup GISA2.0 \cup (\text{Imp-ESA}_{LC}) \cup (\text{Imp-ESRI\_LC}) \tag{2}$$

3.2.2 Training areas of wetland

205   In this work, wetlands are divided into four inland subcategories (swamp, marsh, river/lake flats, and saline) and
206 three coastal wetland subcategories (mangrove, salt marsh, and tidal flats in **Table 2**). Because coastal wetlands have
207 a more pronounced zonation, and the global coastal wetland mapping have make great progresses while the works of
208 global inland wetland mapping is still sparse (Wang et al., 2023), thus, the generation of wetland training candidate
209 areas further distinguishes between inland and coastal wetlands.
210   The time-series GWL_FCS30D wetland product covering the period of 2000–2022 is used to derive the inland
211 wetland training candidate areas (Zhang et al., 2024b). Because temporally stable areas achieve higher accuracy
212 (Yang and Huang, 2021), a temporally stable analysis is applied to the GWL_FCS30D, and only those stable areas
213 where wetland subcategories do not change during 2000–2022 are retained (yielding the training area,
214 *TrainCanArea_Inwet*). Then, because adjacent land-cover areas are easier to suffer from the higher misclassifications
215 (Radoux et al., 2014) and to the impact of the satellite geolocation error (Zhang and Roy, 2017), a spatial filter with
216 a local window of 3 pixels × 3 pixels is applied to *TrainCanArea_Inwet* to retain spatially homogeneous areas as the
217 training areas. Further, the integration of multiple wetland products improves sample quality, but there are few high-
218 quality wetland products that have been publicly shared. Only the National Wetland Inventory for 2019 is imported
219 to optimize the swamp and marsh land-cover types in *TrainCanArea_Inwet* over the United States. The areas
220 identified as swamp and marsh in *TrainCanArea_Inwet* and the National Wetland Inventory are retained. The
221 National Wetland Inventory does not identify river/lake flats or saline subcategories.
222   As for the three coastal wetland subcategories, their training areas are generated from the combination of
223 GWL_FCS30D and three coastal wetland products (GMW, GTF30, and GSM10 in **Table 1**). We identify temporally
224 stable coastal wetland areas from GWL_FCS30D, GMW, and GTF30 through time-series analysis and label them
225 GWL_stable, GMW_stable, and GTF_stable. Then, we intersect GWL_stable with GMW_stable to generate
226 mangrove forest training areas and intersect GWL_stable with GTF_stable to generate tidal flat training areas. Next,
227 as the GSM10 only provides salt marsh maps in 2020, the salt marsh training areas are selected as the intersection
228 between GWL_stable and GSM10. The mangrove forest, tidal flat, and salt marsh training areas are grouped as
229 *TrainCanArea_Cowet*.
230   Last, the maximum wetland boundary (*MaxBound_wet*) is also necessary for the subsequent identification of
231 training areas for non-wetland natural land-cover types. *MaxBound_wet* is determined as the union of the five global
232 wetland products:

$$MaxBound_{wet} = GWL\_FCS30D \cup NWI \cup GMW \cup GTF30 \cup GSM10 \tag{3}$$

3.2.3 Training areas of non-wetland natural land-covers

Many previous works have emphasized that these spatiotemporally stable areas always performed higher mapping accuracy (Zhang and Roy, 2017; Zhang et al., 2024c). In this work, the time-series global 30-m land-cover dynamic product (GLC_FCS30D), covering the period of 1985–2022 is used. The product uses a classification system like the one used in this work. Specifically, three measures are taken to identify spatiotemporally stable areas of non-wetland natural land-cover types from GLC_FCS30D: 1) A time-series consistency analysis is applied to the GLC_FCS30D, and only stable areas during 1985–2022 will be retained as *TrainCanArea_NLCs*. 2) The $MaxBound_{imp}$ and $MaxBound_{wet}$ are imported to mask the *TrainCanArea_NLCs*, i.e., the training areas for non-wetland natural land-cover types should be located outside of $MaxBound_{imp}$ and $MaxBound_{wet}$. The aim of this step is to minimize confusion between non-wetland natural land-cover types and these two other land-cover types. 3) A morphological erosion filter with a local window of 3 pixels × 3 pixels is used to find the spatially homogeneous areas for non-wetland natural land-cover types. In addition, it should be noted that the TrainCanArea_NLCs represents the stable areas during 1985-2022, and there is still one-year interval with the land-cover mapping year in 2023. Fortunately, the ongoing updating of GLC_FCS30D is still in progress, the land-cover change masks during 2022-2023 have been finished, and which are also used to remove these changed and low-confidence areas.

As mentioned in Section 2.2.4, the training areas for tree-cover cropland (oil palm, orchards, etc.) from the GLC_FCS30D do not cover the globe. These training areas are therefore divided into herbaceous rainfed cropland and tree- or shrub-cover cropland. Because the global oil palm and global plantation datasets provide the plantation years of oil palm and orchards at 30 m, we overlap the training areas of rainfed cropland, oil palm, and orchard plantation from the global plantation dataset to extract the training areas for tree-cover cropland. Then, to minimize error, the tree-cover cropland training areas are further filtered using a local window of 3 pixels × 3 pixels to ensure spatial homogeneity of tree-cover cropland training areas.

3.2.4 Generating a globally distributed training pool from stratified sampling

Although we take a series of measures to ensure training area quality (including: *TrainCanArea_urban, TrainCanArea_rural, TrainCanArea_Inwet, TrainCanArea_Cowet,* and *TrainCanArea_NLCs*), how to generate training samples from the training areas needs to address the following two aspects.

First, the distribution and balance of training samples greatly affect the subsequent land-cover classification (Ghorbanian et al., 2020; Jin et al., 2014; Mellor et al., 2015; Pelletier et al., 2017; Zhu et al., 2016). There are two options to allocate the sample distribution: equal or area-fraction allocation (Zhang et al., 2021). Equal distribution means that all land-cover types have the same number of training samples, i.e., the sample sizes of sparse land covers will be augmented while those of the abundant land covers will be suppressed. In contrast, area-fraction distribution allocates the sample size according to the land-cover area of each type, that is, abundant land covers have larger sample sizes while sparse land-cover types have smaller sample sizes (Zhu et al., 2016). Because impervious surfaces and wetlands are sparser than natural land-cover types and are independently generated, equal-distribution allocation is suitable to enhance the training samples' ability to characterize these two land-cover types. As for the non-wetland natural land-covers, the area-fraction allocation is more appropriate for the non-wetland natural land-cover types because we want to optimize results for all non-wetland natural land-cover types rather than a single land-cover type. Meanwhile, to avoid sample size imbalance in the area-fraction allocation, maximum and minimum sample sizes of 8000 pixels and 600 pixels are chosen for the abundant and sparse land-cover types, respectively (suggested by the work of Zhu et al. (2016)).

Second, most high-quality training samples (except for those for impervious surfaces) are derived from the 30-m training areas, so there is also a need to reduce the 30-m training samples to 10-m samples to achieve a global 10-m land-cover map. In this work, the "metric centroid" method is adopted, which had been used to downscale 500-m training samples from MCD12Q1 to 30-m in the work of Zhang and Roy (2017). Specifically, as each 30-m pixel

corresponds to 3 × 3 10-m pixels, we first find the centroid from these nine pixels as $P_{centroid}$ through spectral averaging, and then the point with the smallest absolute distance with $P_{centroid}$ was chosen as the optimal downscaled 10-m sample point [**Eq. (4)**].

$$P_i = \underset{i}{\text{argmin}}\left(\left|\boldsymbol{\rho}_{P_i} - \boldsymbol{\rho}_{P_{centroid}}\right|\right), \boldsymbol{\rho}_{P_{centroid}} = \frac{1}{9}\sum_{j=1}^{9}\frac{\boldsymbol{\rho}_{P_j}}{9} \tag{4}$$

Where $\boldsymbol{\rho}_{P_i}$ is the spectra value of composited Sentinel-2 training features (See Section 3.3) at pixel P_i. If more than one point in the nine pixels has the same minimum absolute distance, then we pick randomly from among them.

3.3 Compositing multisourced training features

In addition to high-confidence training samples, how to generate these multisource training features is also important (Dong et al., 2015; Jin et al., 2023; Yang and Huang, 2021). In this work, we composite multitemporal optical and SAR information from Sentinel-1 and Sentinel-2 time-series observations. First, because of the overlapping orbits of the satellites and the effects of clouds and shadows, there are substantial differences in the clear-sky observations in different regions. Compositing methods help to obtain dimensionally consistent spectral-phenological features. The percentile-based statistical multitemporal compositing method attracts attention because of its robustness, efficiency, and simplicity (Azzari and Lobell, 2017). The basic principle of This this method is to rearranges intra-annual time-series reflectance according to mathematical magnitude and take the corresponding quartiles to reflect the phenological variation of the time-series and suppress the noise interference such as clouds and shadows (Hansen et al., 2014). Some previous studies have also demonstrated its ability to flexibly balance noise removal and signal retention, reflecting the surface normality and capturing peak features (e.g., high percentile), adapting to different monitoring needs (Hansen et al., 2014; Zhang and Roy, 2017). Thus, in percentile-based compositingin this study, time-series Sentinel-2 images are composited into the 10th, 30th, 50th, 70th, and 90th percentiles for their 10 optical bands from visible to shortwave infrared and three typical indexes [NDVI, NDWI, and LSWI in **Eq. (5)**] using the percentile-based compositing method. The 10th and 90th percentiles are selected to represent the poles of time-series variations and also suppress the effects of residual cloud and shadow, and the other three percentiles can partly reflect the phenological variations (Xie et al., 2020). Meanwhile, another major advantage of 10-m Sentinel-2 imagery is that it provides clearer textural features, so we generate time-series texture features from the five percentiles in the NIR bands using the gray level co-occurrence matrix. Only the texture features in the NIR band are extracted to avoid redundancy, because of the texture similarity within different spectral bands (Rodriguez-Galiano et al., 2012).

$$NDVI = \frac{\rho_{NIR} - \rho_r}{\rho_{NIR} + \rho_r}, LSWI = \frac{\rho_{NIR} - \rho_{SWIR1}}{\rho_{NIR} + \rho_{SWIR1}} \text{ and } NBWI = \frac{\rho_{green} - \rho_{SWIR1}}{\rho_{green} + \rho_{SWIR1}} \tag{5}$$

where $\rho_{green}, \rho_r, \rho_{NIR}, \rho_{SWIR1}$ are the spectral bands of green, red, NIR, and SWIR1 in the Sentinel-2 imagery.

Then, because SAR signals are sensitive to changes in surface water dynamics and spatial structure, it is also necessary to extract multitemporal SAR features from Sentinel-1 imagery (Bullock et al., 2022; Dabrowska-Zielinska et al., 2018; Zhang et al., 2020). The percentile-based composited method is also used to capture the time-series variabilities of VV and VH at the 10th, 30th, 50th, 70th, and 90th percentiles. In summary, a total of 10 SAR features are composited from time-series Sentinel-1 observations.

Afterward, because some land-cover types are characterized by important topographic distribution (e.g., permanent snow and ice are clustered in high elevation areas, croplands and impervious surfaces usually locate on these flat areas), the topographical variables (slope, aspect and elevation), generated from the resampled ASTER GDEM dataset, are collected into the multisourced training features. It should be noted that some 5 × 5 geographical tiles do not have sufficient Sentinel-1 observational data in 2023 since Sentinel-1B is retired in 2022, the corresponding tiles use only Sentinel-2 and topographic data.

3.4 Hierarchical land-cover mapping

A major advantage of hierarchical land-cover mapping is the ability to improve the characterization of complex land-covers with independent models, the major flowchart is illustrated at the Figure 2. In this work, we first separate global land-cover types into impervious surfaces and natural land-cover types, then identify the wetlands from among the natural land-covers, and finally classify the remaining non-wetland natural land-cover types into 20 land-cover subcategories.
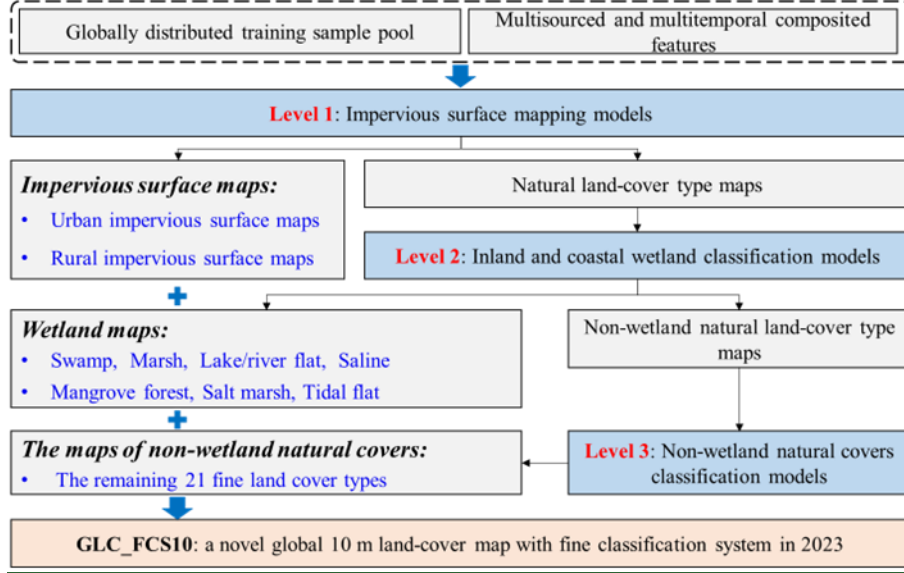
Figure 2. The detailed flowchart of hierarchical land-cover mapping algorithm by integrating globally distributed training samples and multisourced composited features.

3.4.1 The separation of impervious surfaces and natural surfaces

To separate impervious surfaces and natural surfaces, we rely on the globally distributed training samples (Section 3.2.4) and the combination of multitemporal optical and SAR features. Specifically, because we divide impervious surfaces training samples into rural and urban samples and design the equal distribution to enhance the training samples' ability to characterize impervious surfaces. The ratio of urban samples, rural samples, and natural surfaces is 1:1:1 for each 5 × 5 geographical tile. Meanwhile, in terms of the sample size of each class, some previous studies have quantified the relationship between sample size and mapping accuracy (Foody, 2009; Li et al., 2014), and suggested a minimum size of 600 and maximum size of 8000 for these sparse and abundant land-cover types (Zhu et al., 2016). In this study, after considering the trade-off between sample representativeness with mapping efficiency, the sample size of each class was selected as 5000, which was also consistent with the work of Zhang et al. (2022) in monitoring the impervious surface dynamics.

Then, wWe split the globe into 984 5 × 5 geographical tiles (approximately 556 km × 556 km on the equator, illustrating on the Figure S1), because some studies emphasized that the local adaptive modeling usually achieves better mapping accuracy than single land-cover global modeling (Zhang et al., 2021), and previous works of Zhang and Roy (2017) and Zhang et al. (2019) have explained that the training samples of sparse land-cover types in a small geographical grid were usually missed or greatly sparse. Thus, after balancing the training sample volume, mapping accuracy, and the limitation of GEE platform, the local modeling tile size of 5 × 5 , similar to the works of (Zhang et al., 2021; Zhang et al., 2024c), were used. Then, Wwhen building the training model for each 5 × 5 geographical tile, we also import training samples within their spatial neighborhood of 3 × 3 tiles to ensure spatial consistency over the adjacent tiles. Since the $MaxBound_{imp}$ (Eq. (2)) provides the maximum potential areas of impervious surfaces because of the overestimation problem of Imp-ESRI_LC (Wang et al., 2024; Xu et al., 2024b), all identified impervious surfaces should be within the $MaxBound_{imp}$. Afterward, we can produce 984 5 × 5 impervious surface

and natural land cover maps using the local adaptive modeling strategy. In addition, although we divide the training samples into urban and rural samples, there is serious confusion between urban and rural areas in the classification maps because they share similar spectral and SAR characteristics. We therefore consider the two subcategories to be inseparable at the classification stage. Correspondingly, inspired by the work of Li et al. (2020) who used the cellular automata and morphological approaches to accurately capture urban boundaries, this method is also applied in this work to distinguish urban and rural impervious surfaces.

Notably, in terms of the selection of classifier at the local adaptive modeling, tThe random forest classification model (including the later section 3.4.2 and 3.4.3) is selectedused. The random forest has some advantages over other traditional classifiers, such as managing high-dimensional data more efficiently, having higher robustness, being insensitive to parameter settings, and avoiding overfitting problems effectively (Belgiu and Drăguţ, 2016; Breiman, 2001). In terms of its parameter settings, the random forest only has two adjustable parameters, and the variations of these two parameters have little effect on the performance of the random forest model (Du et al., 2015; Gislason et al., 2006), thus, the default parameter settings are applied to train the random forest models on the GEE platform.

3.4.2 The separation of wetland and non-wetland natural land-cover types

In terms of how to identify the fine wetland subcategories from natural land-covers, we use the stratified wetland mapping algorithm to independently distinguish coastal wetlands and inland wetlands. Wetlands are divided into four inland and three coastal wetland subcategories (in **Table 2**), and equal-distribution sampling is used to enhance the training samples' ability to characterize wetlands. Additionally, since some non-wetland land-cover types also reflected the similar spectral characteristics with the wetlands, for example, the swamp and the forest/shrubland shared similar vegetation signalsspectra during the peak growth period, while the marsh and cropland/grassland exhibited the characteristics of herbaceous vegetations, and the river flats also performed the spectral characteristics of bare land during the dry seasons (Zhang et al., 2023b). Thus, tThe approximate ratio of inland wetlands, coastal wetlands, and non-wetlands (including water body, forest/shrubland, cropland/grassland, bare land, and others) is 4:3:5 in areas where they coexist. Then, because coastal wetlands have a more pronounced zonation, we can obtain their maximum coverage through the union of some previous coastal wetland products, as Eq. (6).

$$MaxBound_{Cos\_wet} = GWL\_FCS30D\_Coastal \cup GMW \cup GTF30 \cup GSM10 \qquad (6)$$

When building the wetland random forest classification models for each 5×5 geographical tile, we first train the coastal wetland classification model using the coastal wetland and non-wetland training samples within their spatial neighborhood of 3×3 tiles, and combine multisourced training features to identify the spatial distribution of coastal wetlands within the $MaxBound_{Cwet}$; i.e., all coastal wetland pixels should be within the $MaxBound_{Cwet}$, otherwise, they would be corrected.

Afterward, the inland wetland and non-wetland training samples are used to train another random forest classification model, and the remaining natural land-cover types are further classified as four inland wetland subcategories and non-wetland natural land-cover types using the inland wetland classification model.

3.4.3 Mapping of non-wetland natural land-cover types

After classifying the impervious surface and wetlands using the hierarchical land-cover mapping, we now need to classify the remaining non-wetland natural land-cover types. Like the previous mapping processes, the local adaptive random forest models are trained for each 5×5 geographical tile using the corresponding training samples within the spatial neighborhood of 3×3 tiles. The non-wetland natural land-cover types are classified through a combination of trained random forest models and multisource training features. Lastly, after overlapping the hierarchical maps for impervious surface, wetland, and non-wetland natural land-cover types, we can obtain 10-m land-cover maps with a fine classification system.

3.5 Accuracy assessment and cross-comparison

To comprehensively assess the performance of our developed GLC_FCS10 products, a globally distributed validation dataset and one third-party validation dataset are collected to quantify the accuracy metrics. First, the global validation dataset, guided by the work of (Zhao et al. (2023), is collected through stratified random sampling and visual interpretation from high-resolution remote sensing imagery in 2023. Figure 2 3 illustrates the spatial distribution of the global validation dataset; it contains 56121 globally distributed validation points and covers 16 land-cover types. Next, the Land Cover Monitoring, Assessment, and Projection Collection (LCMAP) validation dataset (called LCMAP_Val), as a national third-party validation dataset, contains 16082 nationally distributed validation points during 1985–2021 (Stehman et al., 2021). In this work, the LCMAP_Val in 2021 is also updated to 2023 through visual interpretation. Afterward, the confusion matrix and four accuracy metrics are calculated, including: the overall accuracy (O.A.) and kappa coefficient (measuring the comprehensive performance) and the producer accuracy (P.A.), and the user accuracy (U.A.), which measure the commission and omission errors for each land-cover type to quantify the accuracy of GLC_FCS10 (Foody and Arora, 2010; Liu et al., 2007; Nelson et al., 2021).
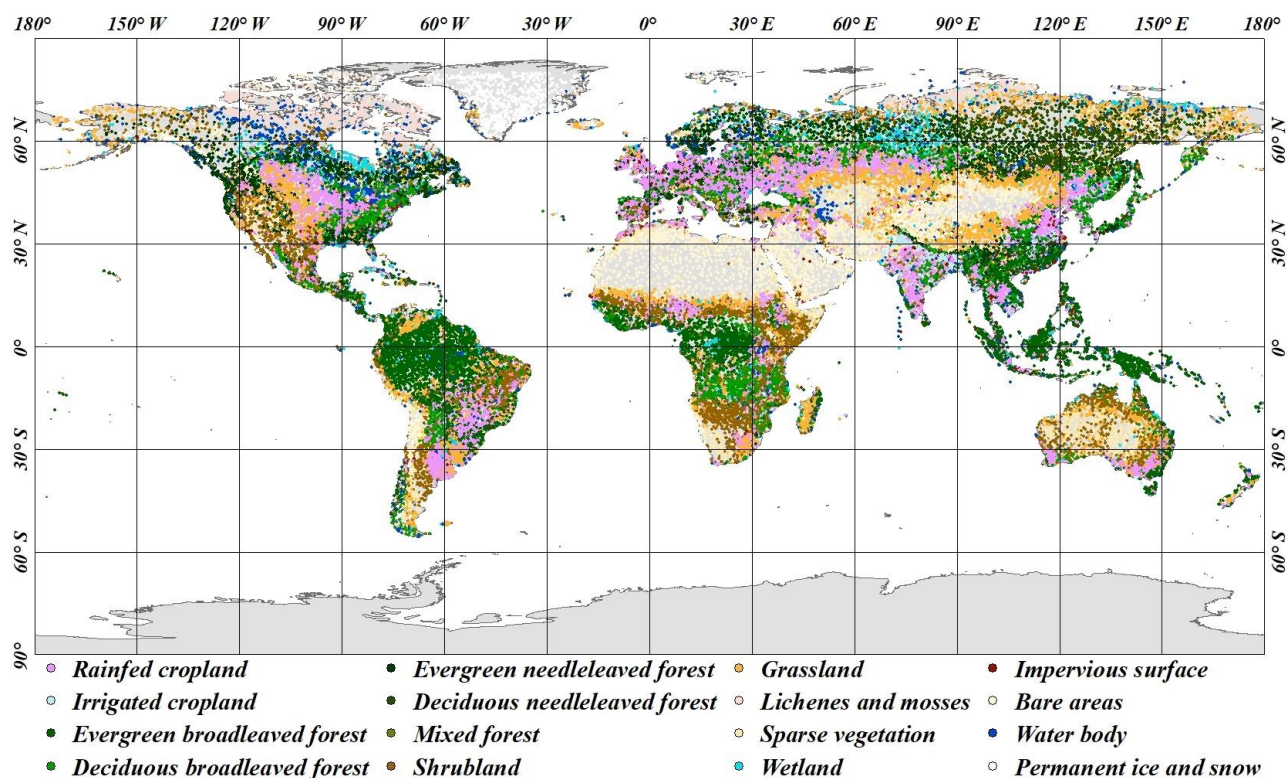
Figure 2 3. The spatial distribution of global validation samples containing 16 land-cover types in 2023.

In addition, to qualitatively investigate the performance of GLC_FCS10, three global 10-m land-cover products [ESRI_LC (Karra et al., 2021), ESA WorldCover (Zanaga et al., 2021), and FROM_GLC10 (Gong et al., 2019)], and one 30-m land-cover product [GLC_FCS30 (Zhang et al., 2021)] are collected as comparative products. None of these five data products have been updated to 2023. Their latest available data will be collected for our comparative analysis.

4. Results and discussions

4.1 Overview of the GLC_FCS10 maps

Figure 3 4 illustrates the spatial distribution of the GLC_FCS10 land-cover maps with 30 fine land-cover types in 2023. Overall, it accurately charactersizes global land-cover patterns, i.e., forests concentrate in tropical rainforest

413 regions and cold temperate forest zones in the northern hemisphere, cropland is found in low-lying plains areas such
414 as the North China Plain, Central Plains of the United States, Central Eurasia, and bare land and grassland are
415 distributed in arid and semiarid areas. Meanwhile, because a characteristic of the GLC_FCS10 is its diverse
416 classification system, we can see that broadleaved forests are found in low- and medium-altitude regions, while
417 needle-leaved forests are distributed in cold temperate zones as well as in high-altitude areas.
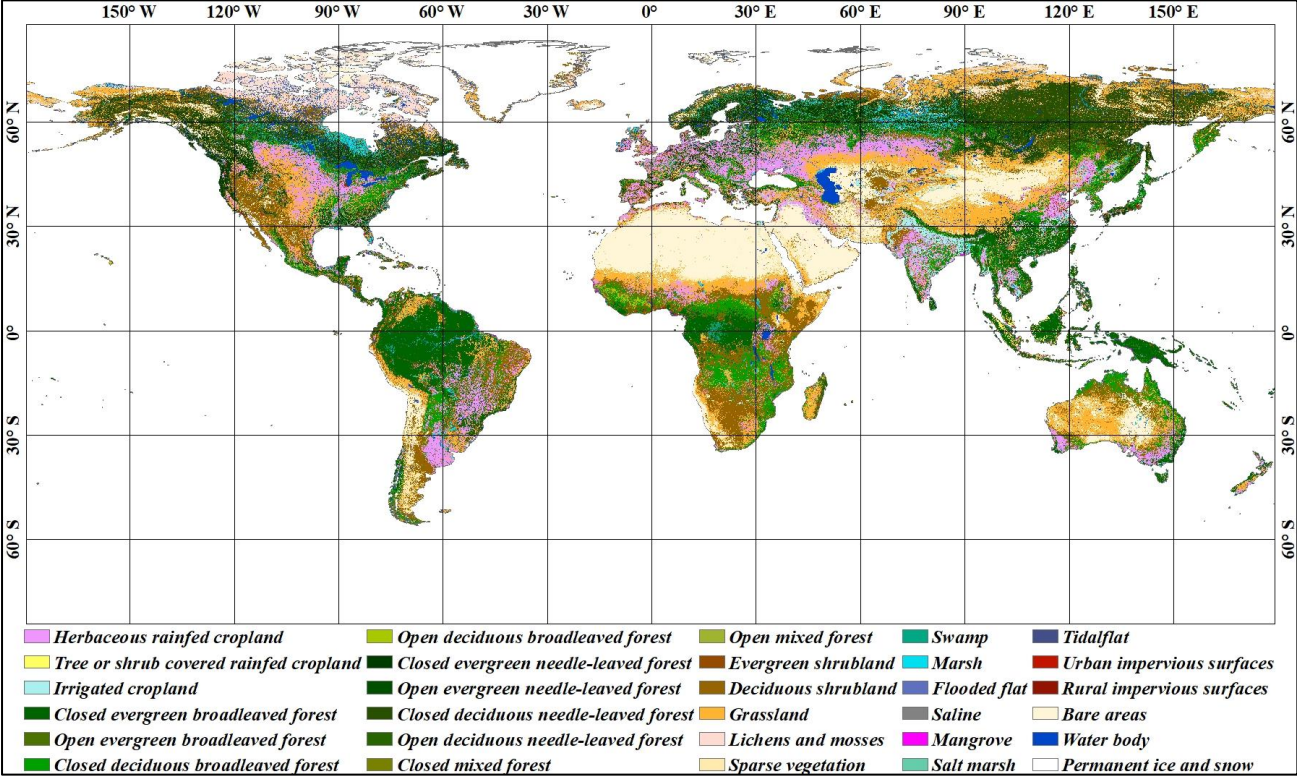
419 **Figure 3~~4~~**. Spatial distribution of the 30 fine land-cover types in GLC_FCS10 land-cover map~~s~~ in 2023.

4.2 Accuracy assessment

4.2.1 Global-scale accuracy assessment

422 Table 3 presents the confusion matrix between GLC_FCS10 and the 56121 globally distributed validation points
423 for 10 major land-cover types (corresponding to the basic classification system in Table 2). Overall, GLC_FCS10
424 achieves an O.A. of 83.16% and a kappa coefficient of 0.789. For specific land-cover types, permanent snow and ice,
425 water bodies, forest, impervious surfaces, and cropland perform the best, with the corresponding U.A. and P.A. values
426 approximating or exceeding 90%. Their high accuracies stem from the distinct spectral properties inherent to water
427 bodies and permanent ice and snow, the abundant coverage of cropland and forest, and hierarchical land-cover
428 mapping for impervious surfaces. However, shrubland, grassland, tundra, and wetlands suffer obvious
429 misclassifications, in which the shrubland has the lowest U.A. of 67.04% and wetland has the lowest P.A. of 53.69%.
430 There are considerable confusions between shrubland, grassland, and bare areas because they share similar spectral
431 characteristics and coexist in arid and semiarid areas. Wetlands have the lowest P.A. due to the confusions between
432 wetlands, water bodies, forest, and grassland. Wetlands have complicated and heterogeneous spectral and temporal
433 variations, thus, the swamp subcategory is easily confused with forest, and the marsh subcategory shares spectral
434 characteristics with grasslands (Zhang et al. (2023b).

435 **Table 3**. The confusion matrix between GLC_FCS10 and the globally distributed validation dataset for 10 major
436 land-cover types.

	Crop	Forest	Shrub	Grass	Tundra	Wetland	Impervious	Barren	Water	Ice-Snow	Total	U.A.
Crop	8442	339	588	768	0	53	39	46	9	0	10284	82.09
Forest	161	18342	1191	189	0	250	2	12	4	0	20151	91.02
Shrub	190	701	4091	922	12	72	4	109	1	0	6102	67.04
Grass	673	255	275	5817	33	170	7	391	4	1	7626	76.28
Tundra	0	25	78	153	805	2	0	61	0	0	1124	71.62
Wetland	10	74	136	100	14	946	1	23	30	0	1334	70.91
Impervious	20	6	11	28	0	1	902	5	0	0	973	92.70
Barren	66	5	187	544	24	29	6	3882	3	13	4759	81.57
Water	2	6	9	4	0	239	1	25	2328	0	2614	89.06
Ice-Snow	0	1	1	33	0	0	0	5	1	1113	1154	96.45
Total	9564	19754	6567	8558	888	1762	962	4559	2380	1127	56121	
P.A.	88.27	92.85	62.30	67.97	90.65	53.69	93.76	85.15	97.82	98.76		
O.A.							83.16					
Kappa							0.789					

437   To intuitively understand the spatial distribution of the GLC_FCS10 accuracy metrics, Fig. 4̶5 presents the
438 spatial variations of O.A. and the kappa coefficient among 30 climate zones from Köppen climate zones. There is
439 high consistency of the O.A. and kappa coefficient within the spatial patterns, i.e., some climatic transition zones,
440 land-cover heterogeneity zones, cloud-contaminated tropical zones, and small subdivisions tend to have lower
441 accuracy (below 80%). Conversely, some homogeneous zones (such as Greenland and the Sahara Desert) and forest-
442 or cropland-rich zones (such as the east-central United States, central Eurasia, and East Asia) achieve the high O.A.
443 and kappa coefficient.

444
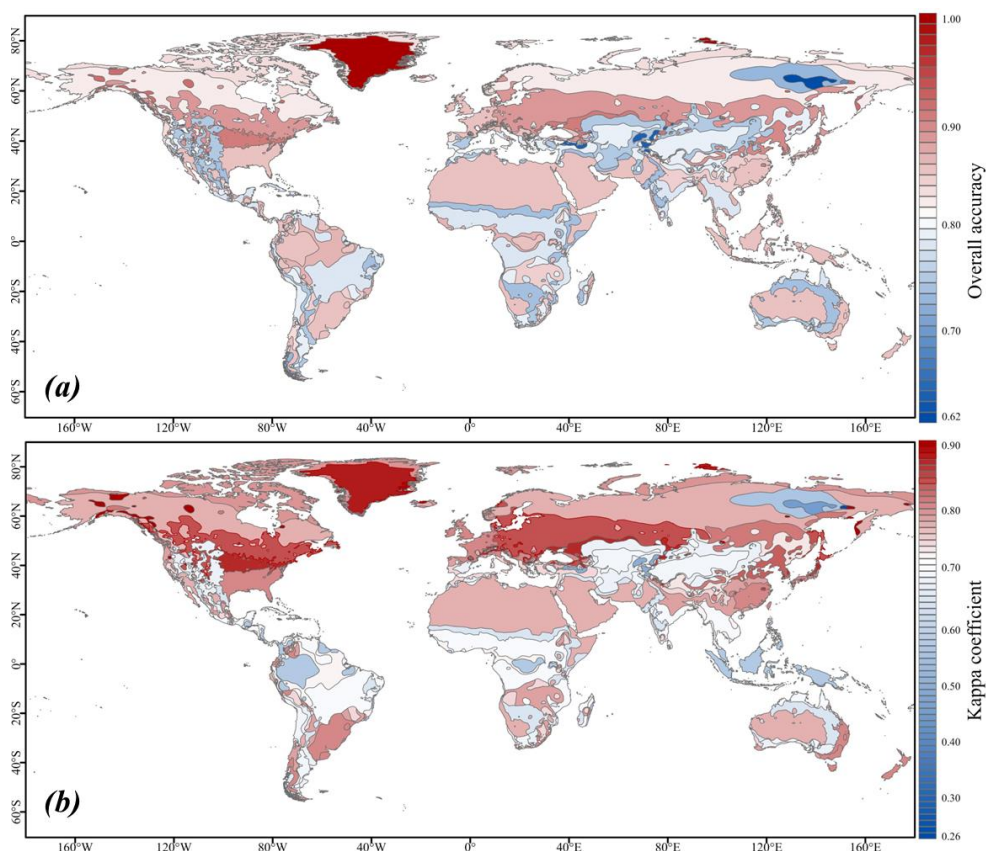
445 **Figure** 4̶5. (a) Regional O.A. and (b) kappa coefficient of the GLC_FCS10 land-cover map̶s among various Köppen
446 climate zones (http://koeppen-geiger.vu-wien.ac.at/) using the globally distributed validation points.

Table 4 further analyzes the confusion matrix between GLC_FCS10 and the global validation dataset with 16 land-cover types (refining the forest and cropland subcategories). Under this fine validation system, the GLC_FCS10 achieves an O.A. of 76.45% and a kappa coefficient of 0.736, which are reduced by 6.71% and 0.053, respectively, from the metrics in Table 3. This reduction is due to confusion between the finer land-cover subcategories; e.g., forests have a U.A. value of 91.02% in Table 3, but when broken down into five forest subcategories the average U.A. value drops to 68.52%. Taking mixed forest as an example, it has a low accuracy of only 44.17%, of which the proportions misclassified as evergreen broadleaved forest (EBF), deciduous broadleaved forest (DBF), evergreen needleleaved forest (ENF), and deciduous needleleaved forest (DNF) are 5.34%, 7.77%, 27.18%, and 5.83%, respectively. Higher likelihoods of confusion exist for closely related land-cover subcategories; e.g., the highest proportion of misclassification in EBF is in DBF, and rainfed cropland is easily misclassified as irrigated cropland, shrubland, or grassland. Previous research also demonstrated that considerable misclassifications occur between similar land-cover types (Homer et al., 2020; Wickham et al., 2021; Zhang et al., 2021; Zhang et al., 2024c).

Table 4. The confusion matrix between GLC_FCS10 and the globally distributed validation dataset for 16 land-cover types.

	RCP	ICP	EBF	DBF	ENF	DNF	MF	SHB	GRS	LMS	SPV	WET	IMP	BAL	WTR	SNW	Total	U.A.
RCP	7575	302	134	137	21	13	6	574	746	0	10	24	31	35	6	0	9614	78.79
ICP	121	444	19	7	2	0	0	14	22	0	1	29	8	0	3	0	670	66.27
EBF	138	0	7263	842	289	59	48	429	70	0	0	140	1	1	2	0	9282	78.25
DBF	21	1	375	3955	235	149	61	482	52	0	0	40	0	1	0	0	5372	73.62
ENF	0	0	191	129	2535	533	11	138	28	0	0	51	1	3	1	0	3621	70.01
DNF	1	0	0	77	122	1278	4	127	37	0	1	16	0	6	1	0	1670	76.53
MF	0	0	11	16	56	12	91	15	2	0	0	3	0	0	0	0	206	44.17
SHB	184	6	60	440	52	140	9	4091	922	12	40	72	4	69	1	0	6102	67.04
GRS	654	19	24	109	21	98	3	275	5817	33	232	170	7	159	4	1	7626	76.28
LMS	0	0	0	6	1	18	0	78	153	805	18	2	0	43	0	0	1124	71.62
SPV	40	3	0	2	1	2	0	0	0	11	266	6	1	0	1	3	336	79.17
WET	8	2	29	9	9	27	0	136	100	14	12	946	1	11	30	0	1334	70.91
IMP	14	6	4	1	0	1	0	11	28	0	0	1	902	5	0	0	973	92.70
BAL	20	3	0	0	0	0	0	187	544	13	118	23	5	3498	2	10	4423	79.09
WTR	2	0	1	1	1	1	2	9	4	0	0	239	1	25	2328	0	2614	89.06
SNW	0	0	0	1	0	0	0	1	33	0	0	0	0	5	1	1113	1154	96.45
Total	8778	786	8111	5732	3345	2331	235	6567	8558	888	698	1762	962	3861	2380	1127	56121	
P.A.	86.30	56.49	89.55	69.00	75.78	54.83	38.72	62.30	67.97	90.65	38.11	53.69	93.76	90.60	97.82	98.76		
O.A.								76.45										
Kappa								0.736										

Note: RCP: rainfed cropland, ICP: irrigated cropland, EBF: evergreen broadleaved forest, DBF: deciduous broadleaved forest, ENF: evergreen needleleaved forest, DNF: deciduous needleleaved forest, MF: mixed forest, SHB: shrubland, GRS: grassland, LMS: lichens and mosses, SPV: sparse vegetation, WET: wetland, IMP: impervious surface, BAL: bare areas, WTR: water body, SNW: permanent ice and snow

4.2.2 National-scale accuracy analysis using the LCMAP_Val datasets

Table 5 presents the confusion matrix for GLC_FCS10 based on the LCMAP_Val validation points over the America. It should be noted that the LCMAP_Val dataset only contains eight land-cover types and merges shrubland and grassland into one mosaiced land-cover type (grass/shrub). The GLC_FCS10 achieves O.A. of 85.09% and a kappa coefficient of 0.804 using these 16082 national validation points. Regarding the U.A. and P.A., the cropland, forest, water. and grass/shrub land-cover types achieve balanced U.A. and P.A. values approximating or exceeding 80%. In contrast, developed land has the lowest U.A. of 54.26% with high P.A. of 98.85%, mainly because of the difference in definitions of developed land and impervious surfaces. The LCMAP_Val definition of developed land

is broad enough to classify inner-city greenery as developed land as well (Xian et al., 2022), which is considered a vegetation land-cover type in the GLC_FCS10. Barren land has the lowest P.A. value of 31.93%, indicating a high ~~com~~mission error of 68.07%. Most of these misclassifications came from the confusion between barren land and grass/shrub land-cover types. It is noteworthy that the grass/shrub shares similar spectral characteristics with barren, and both of them co-exist in arid regions of the western United States, thus, it is usually difficult to distinguish between the two with high accuracy.

Table 5. The confusion matrix between GLC_FCS10 and the LCMAP_Val dataset.

	Cropland	Forest	Grass/Shrub	Wetland	Impervious	Barren	Water	Ice & Snow	Total	U.A.
Cropland	3445	28	393	6	0	9	2	0	3883	88.72
Forest	7	4621	133	92	0	0	2	0	4855	95.18
Grass/Shrub	368	358	3440	21	1	272	1	0	4461	77.11
Wetland	37	260	30	522	1	0	5	0	855	61.05
Developed	44	69	164	3	344	9	1	0	634	54.26
Barren	1	0	0	10	0	137	1	0	149	91.95
Water	0	2	1	63	2	1	1173	0	1242	94.44
Ice & Snow	0	0	0	0	0	1	0	2	3	66.67
Total	3902	5338	4161	717	348	429	1185	2	16082	
P.A.	88.29	86.57	82.67	72.80	98.85	31.93	98.99	100.00		
O.A.					85.09					
Kappa					0.804					

Figure ~~5~~ 6 illustrates the spatial distribution of O.A. and kappa coefficient values among different Köppen climate zones using the LCMAP_Val validation points over the America. There is notable consistency between O.A. and kappa coefficient in terms of the spatial patterns, i.e., the GLC_FCS10 considerably outperforms the Western U.S. in the Eastern U.S. and has an optimal kappa coefficient of more than 0.8 in the Northeastern U.S. Combined with the climatic distribution, it performs relatively poorly in the arid and semi-arid zones of the Midwestern U.S., mainly attributed to the difficulty in distinguishing between shrubs, grasses, and bare land within the region.
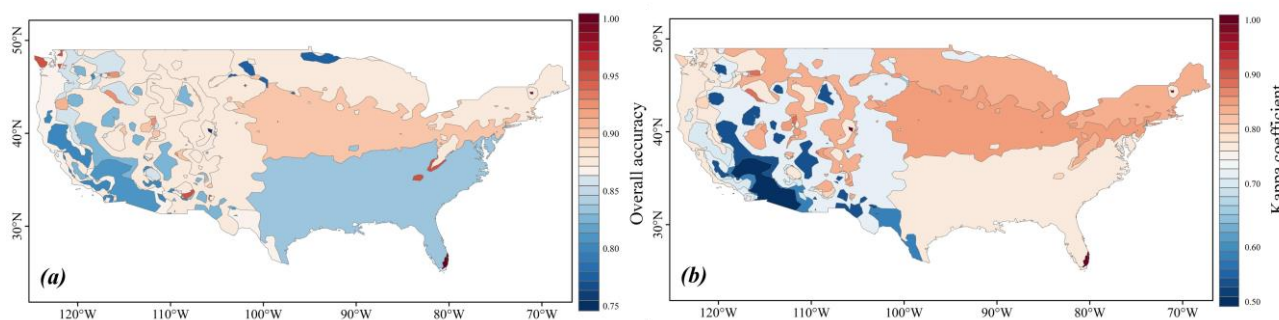
Figure ~~5~~ 6. The spatial distributions of (a) O.A. and (b) kappa coefficient using the LCMAP_Val validation points over the America among various Köppen climate zones.

4.3 Cross-comparisons with previous land-cover products

Table 6 gives quantitative comparisons among GLC_FCS10 and four public global 10- or 30-m land-cover products using the LCMAP_Val dataset. The GLC_FCS10 achieves the highest O.A. of 85.09% and a kappa coefficient of 0.804, followed by the ESA WorldCover (82.34% and 0.760) and ESRI_LC (82.10% and 0.754), while the GLC_FCS30 and FROM_GLC10 have relatively inferior performance, below 80%. Specifically, in terms of the P.A., U.A. and F1-score, we can find that: 1) all five products achieve superior performance for water with corresponding P.A., U.A. and F1 score values of more than 90%. 2)The GLC_FCS10 and ESA WorldCover have

495 advantages over other products for cropland and forest (with F1 scores exceeding 85%). The ESRI_LC F1 scores for
496 cropland, forest, and grass/shrub exceed 80%. 3)All five products faced challenges for wetlands and barren land due
497 to their complicated spectral characteristics. Taking wetlands as an example, the GLC_FCS10 achieves the highest
498 F1 score of 66.63%, with most other products below 50%. The FROM_GLC10 has the lowest F1 score of 7.58%. 4)
499 As stated in Section 4.2.2, the difference in definitions for developed land and impervious surfaces mean that all
500 land-cover products have lower U.A. than P.A. values for developed land, i.e., they cannot identify inner-city greenery
501 as impervious surfaces.

502 **Table 6.** Comparisons among GLC_FCS10 and four other comparative products using the LCMAP_Val dataset.

		Cropland	Forest	Grass/Shrub	Wetland	Developed	Barren	Water	Snow	O.A.	Kappa
GLC_FCS10	U.A.	88.72	95.18	77.11	61.05	54.26	91.95	94.44	66.67		
	P.A.	88.29	86.57	82.67	72.80	98.85	31.93	98.99	100.0	85.09	0.804
	F1	88.50	90.67	79.79	66.41	70.06	47.40	96.66	80.00		
FROM_GLC10	U.A.	71.14	87.13	73.70	4.02	41.64	90.50	96.03	100.0		
	P.A.	89.17	82.42	73.47	66.00	85.31	9.30	98.34	50.00	74.31	0.653
	F1	79.14	84.71	73.58	7.58	55.96	16.87	97.17	66.67		
ESA WorldCover	U.A.	86.14	94.51	80.69	13.78	35.49	93.85	97.41	100.0		
	P.A.	93.09	82.00	85.15	88.28	97.20	14.38	98.93	75.00	82.34	0.760
	F1	89.48	87.81	82.86	23.84	52.00	24.94	98.16	85.71		
ESRI_LC	U.A.	90.02	82.84	84.98	10.15	69.36	56.52	97.69	100.0		
	P.A.	80.65	83.05	81.86	69.72	74.38	38.72	98.48	25.00	82.10	0.754
	F1	85.08	82.94	83.39	17.72	71.78	45.96	98.08	40.00		
GLC_FCS30	U.A.	85.78	88.85	75.29	37.68	38.10	73.49	90.79	100.0		
	P.A.	77.39	74.69	84.47	56.09	91.70	20.08	98.14	75.00	77.76	0.699
	F1	81.37	81.16	79.62	45.08	53.83	31.54	94.32	85.71		

503 Figure 6 7 compares GLC_FCS10 with ESA WorldCover, ESRI_LC, GLC_FCS30, and FROM_GLC10 on the
504 East Coast of the United States. Overall, there is the highest consistency between GLC_FCS10 and actual land-cover
505 situations, i.e., wetlands are predominantly found in low-lying river valleys and along the coast, and with a cross-
506 section of forests and cropland due to the undulating topography. Conversely, ESA WorldCover has the largest forest
507 area because some swamps or woody wetlands are labeled as forests (Fig. 6R1 7R1 is an enlargement showing an
508 example). ESA WorldCover also has the smallest impervious surface area because some is misclassified as forest
509 (Fig. 6R2 7R2 is an enlargement showing an example). Thus, ESA WorldCover has low U.A. values of 13.78% and
510 35.49% for wetland and developed land, respectively (Table 6). ESRI_LC has the largest impervious surface area
511 and also identifies some swamps as forest, so it has the lowest P.A. value of 74.38% for developed land. ESRI_LC
512 overestimates impervious surfaces and has obvious omission errors for swamps. FROM_GLC10 has the lowest
513 wetland area, i.e., some swamps are classified as forest and herbaceous wetlands are labeled as water, so it has the
514 lowest U.A. value of 4.02% for wetlands in Table 6. Last, GLC_FCS30 also has omission errors for wetlands (the
515 red rectangle on GLC_FCS30) and lacks spatial details for some small objects (such as small rivers in Fig. 6R1 7R1).
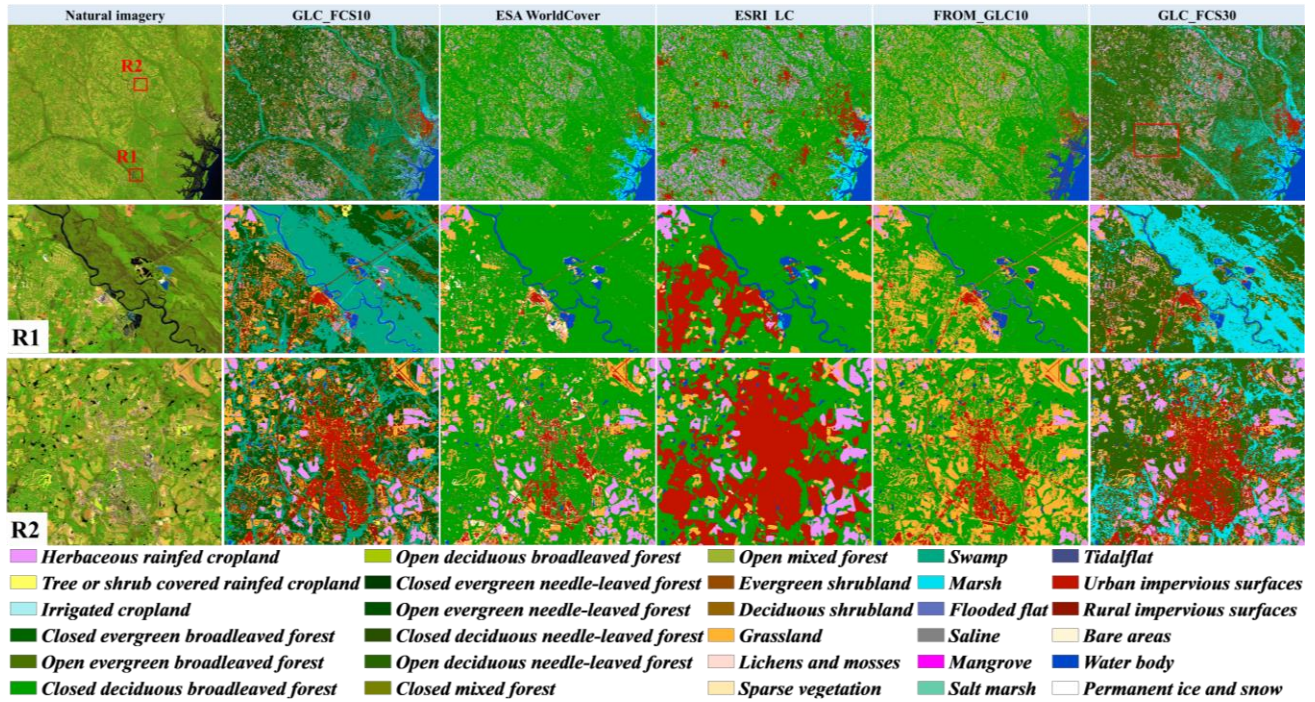
Figure ~~6~~7. Comparisons among GLC_FCS10 and ESA WorldCover, ESRI_LC, GLC_FCS30, and FROM_GLC10 on the East Coast of the United States. Images in the first column are false-color composited from time-series Sentinel-2 imagery.

Figure ~~7~~8 presents comparisons for the moddle reaches of the Yangtze River, China. All land-cover products accurately capture the regional spatial patterns, and GLC_FCS10 and GLC_FCS30 have advantages with the diversity of land-cover types over the other three products. Specifically, Fig. ~~7R1~~8R1 illustrates cross-comparisons for the megacity of Wuhan. ESA WorldCover underestimates and has the lowest impervious surface area, ESRI_LC overestimates and has the highest impervious surface area, and FROM_GLC10 misclassifies some impervious surfaces as grassland (Huang et al., 2022).. Based on the former comparison and previous works (Huang et al., 2022), the ESA WorldCover underestimates these low-density impervious surfaces, the ESRI_LC suffers the overestimation problem on the impervious surfaces, and FROM_GLC10 suffers some misclassificaiton between impervious surfaces and grassland. Fig. ~~7R2~~8R2 shows comparisons over the Payang Lake wetlands. ESA WorldCover captures most marsh wetlands but misses these lake/flooded flats, while ESRI_LC, FROM_GLC10, and GLC_FCS30 have serious omission errors for these wetlands. ESRI_LC misclassifies some marsh wetlands as grassland. Figure ~~7R3~~8R3 illustrates comparisons for mountainous areas. ESRI_LC overestimates impervious surfaces, and GLC_FCS30 misses some small impervious surface objects (roads) due to spatial resolution constraints.
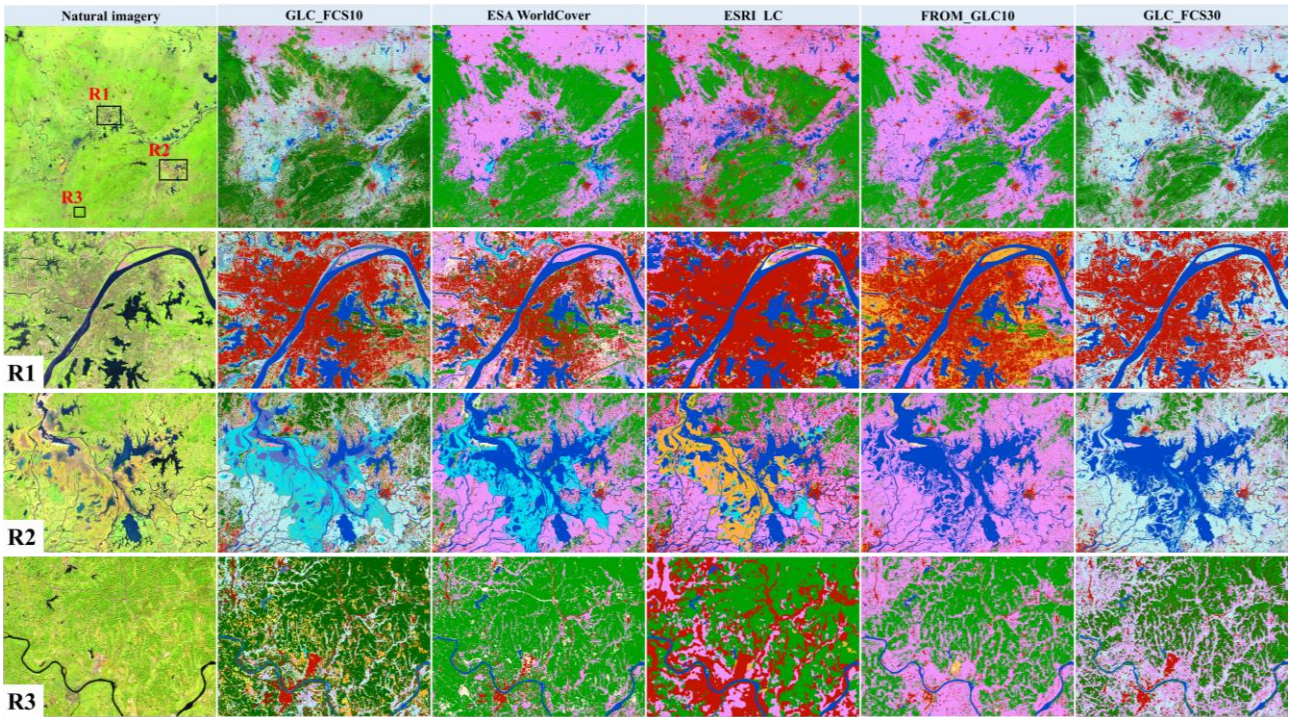
Figure 7̶8. Comparisons among GLC_FCS10 and ESA WorldCover, ESRI_LC, GLC_FCS30, and FROM_GLC10 for the middle reaches of the Yangtze River, China. Images are derived from Sentinel-2 imagery using false-color compositing. The colormap of all land-cover products are same as in Fig. 6.

Because land-cover mapping usually finds tropical areas challenging, Fig. 8̶ 9 shows comparisons for Kalimantan Island, Indonesia. The region has experienced extensive deforestation and oil palm cultivation over the past few decades (Descals et al., 2024). GLC_FCS10, GLC_FCS30, and FROM_GLC10 can capture the spatial patterns of oil palms because they identify oil palms as cropland, while ESA WorldCover and ESRI_LC tend to treat oil palms as forest. Specifically, in Fig. 8R1̶9R1, we can see more regular oil palm plantations due to human activities, while FROM_GLC10 and GLC_FCS30 might overestimate the cropland. ESRI_LC and FROM_GLC have serious omission errors on mangroves and swamps for the local region shown in Fig. 8R2̶9R2, which contains swamp, mangrove, and oil palms,̶, while ESA WorldCover still cannot identify these swamp wetlands and oil palms, and GLC_FCS30 is consistent with GLC_FCS10 in capturing the wetlands and oil palms.
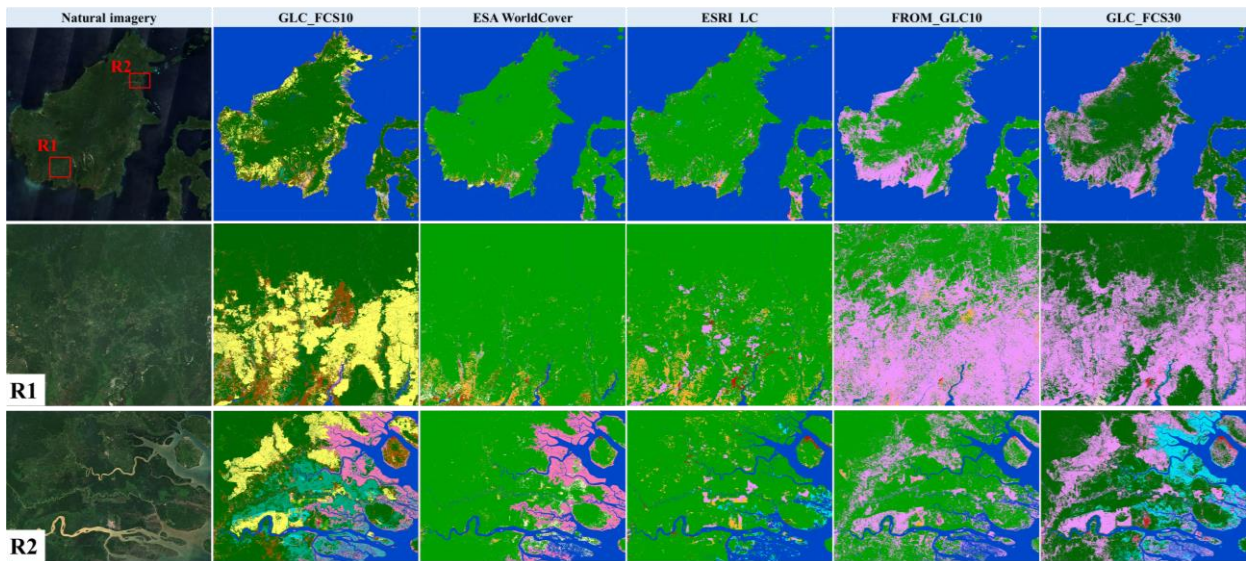
Figure 8̶9. Comparisons between GLC_FCS10 and ESA WorldCover, ESRI_LC, GLC_FCS30, and FROM_GLC10

548 for Kalimantan Island, Indonesia. Images are derived from Sentinel-2 imagery in 2023, and the colormap is the same
549 as in Fig. ~~6~~7.

4.4 The feasibility and benefits of the proposed method for large-area land-cover mapping

4.4.1 The feasibility and advantages of globally derived training samples

A principal difficulty of land-cover mapping is obtaining high-quality training samples (Li et al., 2023; Zhang et al., 2021), in this work, we integrate prior multisource global land-cover products to generate globally distributed training samples. To ensure the confidence of these derived training samples and minimize the classification errors of each prior product, we took the following actions: ~~Spatiotemporal~~ spatiotemporal consistency checking was used to find homogeneous and stable areas. The intersection of multiple land-cover products minimized the influence of classification errors in each product. A morphological erosion filter was applied to reduce the impact of edge-mixing effects. The accuracy assessment partly demonstrates the reliability of these derived training samples, i.e., GLC_FCS10 achieves satisfactory accuracy metrics and outperforms several other land-cover products. Similarly, Zhang et al. (2021) also used the prior global land-cover products to generate the GLC_FCS30 product with satisfactory performance. Due to the large volume of these globally distributed training samples, we selected approximately 10,000 derived samples from the training sample pool in Section 3.2.4. Upon meticulous inspection, we determined that these chosen samples attained an ~~Overall~~ overall ~~Accuracy~~ accuracy (O.A.) of 92.18%, with certain uncertainties existing for shrubland and grassland. This result was in accordance with the earlier analysis presented in Table 3.

Moreover, it is still uncertain whether this small amount of erroneous training samples could impact the performance of land-cover mapping, Fig. ~~9~~10 illustrates the quantitative relationship between the erroneous training samples and the O.A. and kappa coefficients for the basic classification system. Initially, O.A. and the kappa coefficient remain stable as the number of erroneous training samples increases. However, a significant decline occurs when the proportion of erroneous samples exceeds 30%. This indicates that the trained random forest model is robust to the erroneous training samples as long as their proportion remains below 30%. In this work, if the fraction of erroneous samples was kept below 30%, the difference in O.A. is approximately 2% and the decrease in the kappa coefficient is approximately 3%. Gong et al. (2024) also demonstrated that a small number of incorrect samples (approximately 20%) didn't affect the land-cover classification accuracy.
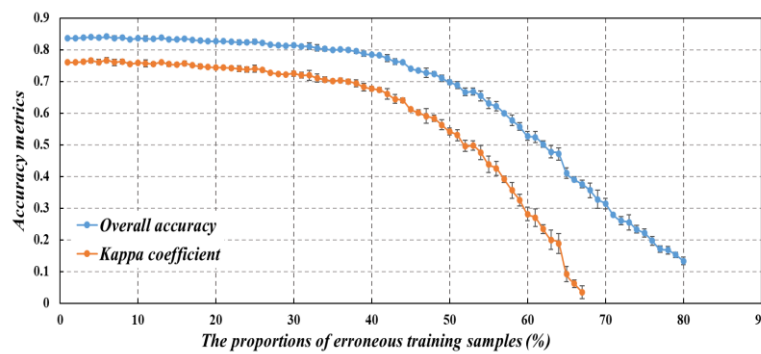
Figure ~~9~~10. A sensitive analysis of kappa coefficient and O.A. with respect to the proportion of erroneous training samples.

4.4.2 The advantages of hierarchical land-cover mapping strategy

One of the novelties of this study is the adoption of the hierarchical land-cover mapping strategy. The accuracy assessment in Table 3 indicates that impervious surfaces have a high U.A. value of 92.70% and P.A. value of 93.76%. The wetlands U.A. and P.A. values are 70.91% and 53.69%, which were superior to those of the other land-cover products in Table 6 and the cross-comparisons in Figs. ~~6~~7–~~8~~9. To intuitively understand the advantage of the

583 hierarchical land-cover mapping strategy, a comparative experiment (***ComExp***) has been designed using the training
584 samples from area-fraction allocation (Fig. ~~10~~11), i.e., the impervious surfaces and wetlands are not classified
585 separately in the middle reaches of the Yangtze River (the comparative site in Fig. ~~6~~7). Overall, the ***ComExp*** is
586 consistent with the GLC_FCS10 spatial patterns and shows some variations in the details. Specifically, in Fig. 10R1,
587 the ***ComExp*** misclassifies some marsh wetlands as herbaceous rainfed cropland. Some lake flats (red rectangles in
588 Fig. ~~10R1~~11R1) cannot be comprehensively captured when compared with the GLC_FCS10. Figure 10R2 gives the
589 comparisons on the impervious surface areas, we can find that the ***ComExp*** has lower impervious surface areas
590 because it misclassifies some bright impervious surfaces as bare areas and some residential areas as vegetated land.
591 In summary, the hierarchical land-cover mapping strategy can increase the ability to characterize specific land-cover
592 types. Sulla-Menashe et al. (2019) also used hierarchical mapping to generate annual global land-cover types for
593 MCD12Q1 and demonstrated its better performance.
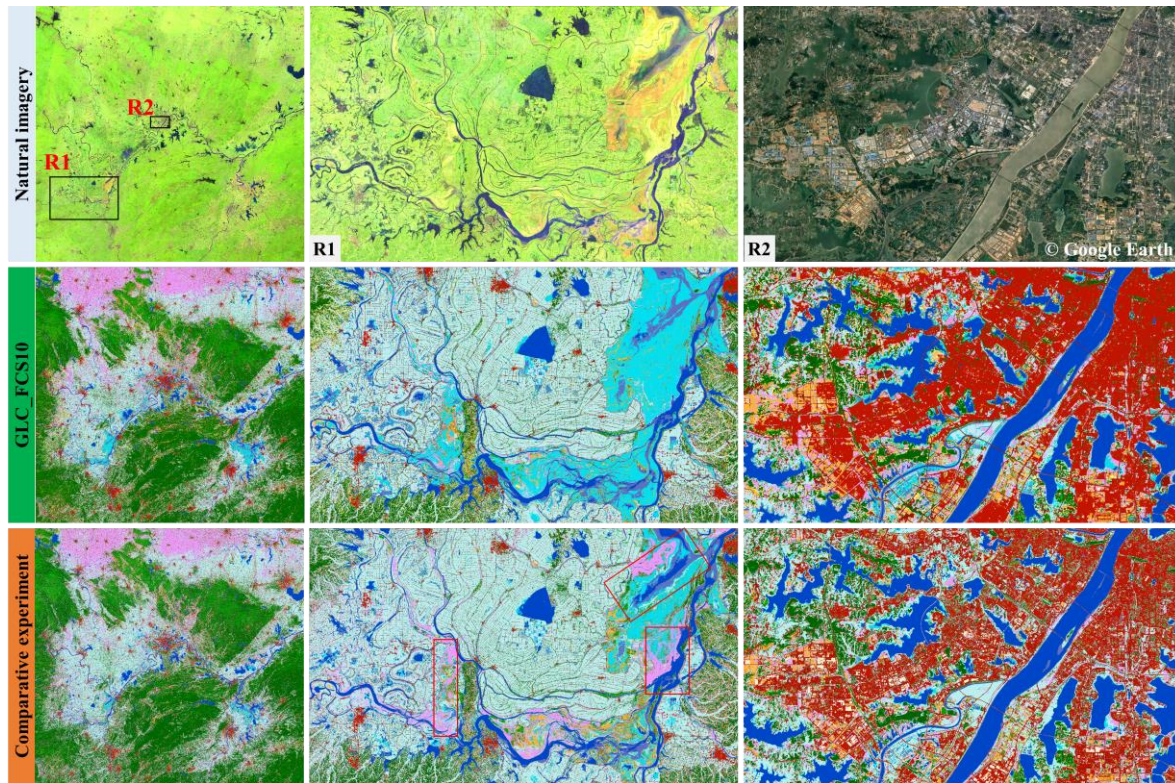
595 **Figure 1~~0~~1**. A comparative experiment on whether to adopt the hierarchical land-cover mapping strategy over the
596 middle reaches of the Yangtze River. Images are composited from Sentinel-2 imagery, and the enlargement came
597 from © Google Earth. The colormap is the same as in Fig. ~~6~~7.

4.5 The limitations and prospects

599 By combining a globally distributed training sample pool and the hierarchical land-cover mapping strategy, a
600 novel GLC_FCS10 product containing 30 category-detailed land-cover types have been produced. GLC_FCS10
601 achieves more accurate performance than several previous products in quantitative and qualitative comparisons
602 (Sections 4.2 and 4.3). However, there are still some limitations or uncertainties regarding the proposed method and
603 the developed products, which will be addressed in our ongoing works. First, although we combined hierarchical
604 land-cover mapping and multisource satellite observations to improve the recognition of complicated land-cover
605 types (impervious surfaces and wetlands), however, it can be found that the accuracy metrics of shrubland, grassland
606 and wetland still have substantial room for improvement. Recently, some efforts have shown that incorporating both
607 climatic and landform factors can enhance the discrimination of grassland areas (Parente et al., 2024) and the
608 combination of Lidar (Light Detection And Ranging) and optical information increases the separability of shrubland

609 and forest (Prošek and Šímová, 2019). Thus, one of the further works will combine multisource information to
610 enhance the ability to recognize complex land-cover types. Meanwhile, although the combination of time-series
611 Sentinel-1 and Sentinel-2 can minimize the effect of clouds and shadows, some high cloud-contaminated areas might
612 be still affected, i.e., mosaic seams may be visible in these special areas. Many previous studies have demonstrated
613 that the harmonization of Landsat and Sentinel-2 can increase the likelihood of clear observations (Claverie et al.,
614 2018), and the advances of deep learning models also improve the land-cover mapping performance on these cloudy
615 areas (Xu et al., 2024a). Thus, how to combine the Landsat imagery and deep learning techniques to further improve
616 the quality of GLC_FCS10 in the persistent cloudy areas will be one of the future works.

617 We collected a globally distributed validation dataset and one third-party validation dataset (LCMAP_Val) for
618 the purpose of quantifying the performance of the GLC_FCS10. However, the accuracy metrics of GLC_FCS10 for
619 the fine classification system (containing 30 land-cover types) is still unknown. Actually, some previous studies have
620 emphasized that collecting a large-area validation dataset is quite challenging (Morales et al., 2023; Tsendbazar et al.,
621 2021; Xu et al., 2020), especially as this study also needed to focus on 30 fine land-cover types. Fortunately, over the
622 past decades, many previous works have collected high-quality validation points at global or regional scales
623 (d'Andrimont et al., 2020; Li et al., 2017; Stanimirova et al., 2023; Stehman et al., 2012; Zhao et al., 2023). Making
624 full use of these prior knowledge bases to refine the globally distributed validation points into 30 fine land-cover
625 types will be another focus for ongoing work. In addition, to objectively understand the accuracy performance of
626 GLC_FCS10, we introduced the LCMAP_Val third-party validation dataset, but the differences in the definition of
627 the classification system still affect the accuracy metrics, such as the higher P.A. and the lower U.A. for the
628 impervious surfaces in Table 5. Therefore, one of the ongoing works would take some measures (such as: semantic
629 similarity (Gao et al., 2020)) to more comprehensively and objectively assess the third-party accuracy metrics of
630 GLC_FCS10.

631 Lastly, in order to maximize the utilization of training samples distributed worldwide and strengthen the
632 classification modeling capacity to capture regional characteristics, the local adaptive modeling strategy (Section 3.4)
633 was applied in each 5 × 5 geographical tile, i.e., the global land-cover maps were produced as 984 independent local
634 adaptive models. There may be a slight spatial discontinuity in some local land-cover maps between neighboring
635 areas even though we introduced spatial neighborhood information into the regional modeling. Thus, further work
636 will take some measures to join global and regional sample modeling to enhance the spatial continuity of global land-
637 cover maps.

5. Data availability

639 In this study, the novel GLC_FCS10 land-cover dataset with the fine classification system in 2023 has been
640 uploaded to the Zenodo platform and can be visually visited at https://zhangxiao-
641 glcproj.users.earthengine.app/view/glcfcs102023maps and freely access at
642 https://doi.org/10.5281/zenodo.14729665 (Liu and Zhang, 2025). To facilitate the use of this dataset, the global
643 GLC_FCS10 dataset has been stored by a total of 983 independent 5 × 5 geographical tiles, and the tile names
644 as "GLC_FCS10_2023_E/W***N/S##," in which the "***" and "##" illustrate coordinates of longitude and latitude
645 at the upper - left corner of the tile data.
646 As the collection of global validation dataset is labor intensive and time-consuming, our globally distributed
647 validation dataset in 2023 will be available upon reasonable request.

6. Conclusion

649 The continuous improvement of satellite techniques and computational capability provides ample opportunity

for high-resolution global land-cover mapping. In this work, we proposed a framework that leverages prior multisource land-cover products, hierarchical land-cover mapping, and local adaptive classification to generate a novel GLC_FCS10 global land-cover product containing 30 fine land-cover types in 2023 from time-series Sentinel-1 and Sentinel-2 imagery on the GEE platform. The GLC_FCS10 was validated to achieve an O.A. of 83.16% and a kappa coefficient of 0.789 using 56121 globally distributed validation points and achieved an O.A. of 85.09% in the United States using a third-party validation dataset. Furthermore, cross-comparisons with several public global high-resolution land-cover products also demonstrated that GLC_FCS10 had advantages on the diversity of land-cover types and capturing spatial details. Therefore, the GLC_FCS10 is a novel global 10-m land-cover product with high accuracy and a fine classification system. It can provide vital support for high-resolution land-cover applications.

Acknowledgment

We extend our sincere gratitude to all the data providers and organizations whose datasets have been utilized in our research paper, the cloud computing power provided by GEE, and the free storage services offered by the Zenodo platform.

Author contributions

The concept and investigation of the project were carried out by LL and XZ. XZ and XC devised the research methodology. TZ, WZ, and MB were responsible for conducting the validation. XZ took the lead in drafting the initial version of the paper. LL and LG engaged in the review and editing process of the paper.

Financial support

This research was supported by the National Key Research and Development Program of China (2024YFF0808301) and the National Natural Science Foundation of China (42201499).

Competing interests

The corresponding author has declared that none of the authors have any competing interests.

References

Azzari, G. and Lobell, D. B.: Landsat-based classification in the cloud: An opportunity for a paradigm shift in land cover monitoring, Remote Sensing of Environment, 202, 64-74, https://doi.org/10.1016/j.rse.2017.05.025, 2017.

Ban, Y., Gong, P., and Giri, C.: Global land cover mapping using Earth observation satellite data: Recent progresses and challenges, ISPRS Journal of Photogrammetry and Remote Sensing, 103, 1-6, https://doi.org/10.1016/j.isprsjprs.2015.01.001, 2015.

Belgiu, M. and Drăguţ, L.: Random forest in remote sensing: A review of applications and future directions, ISPRS Journal of Photogrammetry and Remote Sensing, 114, 24-31, https://doi.org/10.1016/j.isprsjprs.2016.01.011, 2016.

Berger, M., Moreno, J., Johannessen, J. A., Levelt, P. F., and Hanssen, R. F.: ESA's sentinel missions in support of Earth system science, Remote Sensing of Environment, 120, 84-90, https://doi.org/10.1016/j.rse.2011.07.023, 2012.

Blickensdörfer, L., Schwieder, M., Pflugmacher, D., Nendel, C., Erasmi, S., and Hostert, P.: Mapping of crop types and crop sequences with combined time series of Sentinel-1, Sentinel-2 and Landsat 8 data for Germany, Remote Sensing of Environment, 269, 112831, https://doi.org/10.1016/j.rse.2021.112831, 2022.

Breiman, L.: Random Forests, Machine Learning, 45, 5-32, https://doi.org/10.1023/A:1010933404324, 2001.

Brown, C. F., Brumby, S. P., Guzder-Williams, B., Birch, T., Hyde, S. B., Mazzariello, J., Czerwinski, W., Pasquarella, V. J., Haertel, R., Ilyushchenko, S., Schwehr, K., Weisse, M., Stolle, F., Hanson, C., Guinan, O., Moore, R., and Tait, A. M.: Dynamic World, Near real-time global 10 m land use land cover mapping, Scientific Data, 9, https://doi.org/10.1038/s41597-022-01307-4, 2022.

691 Buchhorn, M., Lesiv, M., Tsendbazar, N.-E., Herold, M., Bertels, L., and Smets, B.: Copernicus Global Land Cover
692 Layers—Collection 2, Remote Sensing, 12, 1044, https://doi.org/10.3390/rs12061044, 2020.

693 Bullock, E. L., Healey, S. P., Yang, Z., Houborg, R., Gorelick, N., Tang, X., and Andrianirina, C.: Timeliness in forest
694 change monitoring: A new assessment framework demonstrated using Sentinel-1 and a continuous change detection
695 algorithm, Remote Sensing of Environment, 276, 113043, https://doi.org/10.1016/j.rse.2022.113043, 2022.

696 Bunting, P., Rosenqvist, A., Hilarides, L., Lucas, R. M., Thomas, N., Tadono, T., Worthington, T. A., Spalding, M., Murray,
697 N. J., and Rebelo, L.-M.: Global Mangrove Extent Change 1996–2020: Global Mangrove Watch Version 3.0, Remote
698 Sensing, 14, 3657, https://doi.org/10.3390/rs14153657, 2022.

699 Chen, J., Chen, J., Liao, A., Cao, X., Chen, L., Chen, X., He, C., Han, G., Peng, S., Lu, M., Zhang, W., Tong, X., and Mills,
700 J.: Global land cover mapping at 30m resolution: A POK-based operational approach, ISPRS Journal of Photogrammetry
701 and Remote Sensing, 103, 7-27, https://doi.org/10.1016/j.isprsjprs.2014.09.002, 2015.

702 Claverie, M., Ju, J., Masek, J. G., Dungan, J. L., Vermote, E. F., Roger, J.-C., Skakun, S. V., and Justice, C.: The Harmonized
703 Landsat and Sentinel-2 surface reflectance data set, Remote Sensing of Environment, 219, 145-161,
704 https://doi.org/10.1016/j.rse.2018.09.002, 2018.

705 d'Andrimont, R., Verhegghen, A., Meroni, M., Lemoine, G., Strobl, P., Eiselt, B., Yordanov, M., Martinez-Sanchez, L., and
706 van der Velde, M.: LUCAS Copernicus 2018: Earth Observation relevant in-situ data on land cover throughout the
707 European Union, doi: 10.5194/essd-2020-178, 2020. https://doi.org/10.5194/essd-2020-178, 2020.

708 Dabrowska-Zielinska, K., Musial, J., Malinska, A., Budzynska, M., Gurdak, R., Kiryla, W., Bartold, M., and Grzybowski,
709 P.: Soil Moisture in the Biebrza Wetlands Retrieved from Sentinel-1 Imagery, Remote Sensing, 10, 1979,
710 https://doi.org/10.3390/rs10121979, 2018.

711 Defourny, P., Kirches, G., Brockmann, C., Boettcher, M., Peters, M., Bontemps, S., Lamarche, C., Schlerf, M., and M., S.:
712 Land Cover CCI: Product User Guide Version 2, 2018. 2018.

713 Descals, A., Gaveau, D. L. A., Wich, S., Szantoi, Z., and Meijaard, E.: Global mapping of oil palm planting year from 1990
714 to 2021, Earth Syst. Sci. Data, 16, 5111-5129, https://doi.org/10.5194/essd-16-5111-2024, 2024.

715 Dong, J., Xiao, X., Kou, W., Qin, Y., Zhang, G., Li, L., Jin, C., Zhou, Y., Wang, J., Biradar, C., Liu, J., and Moore, B.:
716 Tracking the dynamics of paddy rice planting area in 1986–2010 through time series Landsat images and phenology-based
717 algorithms, Remote Sensing of Environment, 160, 99-113, https://doi.org/10.1016/j.rse.2015.01.004, 2015.

718 Du, P., Samat, A., Waske, B., Liu, S., and Li, Z.: Random Forest and Rotation Forest for fully polarized SAR image
719 classification using polarimetric and spatial features, Isprs Journal of Photogrammetry & Remote Sensing, 105, 38-53,
720 https://doi.org/10.1016/j.isprsjprs.2015.03.002, 2015.

721 Du, Z., Yu, L., Yang, J., Xu, Y., Chen, B., Peng, S., Zhang, T., Fu, H., Harris, N., and Gong, P.: A global map of planting
722 years of plantations, Scientific Data, 9, https://doi.org/10.1038/s41597-022-01260-2, 2022.

723 Foley, J. A., Defries, R., Asner, G. P., Barford, C., Bonan, G., Carpenter, S. R., Chapin, F. S., Coe, M. T., Daily, G. C.,
724 Gibbs, H. K., Helkowski, J. H., Holloway, T., Howard, E. A., Kucharik, C. J., Monfreda, C., Patz, J. A., Prentice, I. C.,
725 Ramankutty, N., and Snyder, P. K.: Global consequences of land use, Science, 309, 570-574,
726 https://doi.org/10.1126/science.1111772, 2005.

727 Foody, G. M.: Sample size determination for image classification accuracy assessment and comparison, International
728 Journal of Remote Sensing, 30, 5273-5291, https://doi.org/10.1080/01431160903130937, 2009.

729 Foody, G. M. and Arora, M. K.: An evaluation of some factors affecting the accuracy of classification by an artificial neural
730 network, International Journal of Remote Sensing, 18, 799-810, https://doi.org/10.1080/014311697218764, 2010.

731 Friedl, M. A., Sulla-Menashe, D., Tan, B., Schneider, A., Ramankutty, N., Sibley, A., and Huang, X.: MODIS Collection 5
732 global land cover: Algorithm refinements and characterization of new datasets, Remote Sensing of Environment, 114, 168-
733 182, https://doi.org/10.1016/j.rse.2009.08.016, 2010.

734 Gao, Y., Liu, L., Zhang, X., Chen, X., Mi, J., and Xie, S.: Consistency Analysis and Accuracy Assessment of Three Global

30-m Land-Cover Products over the European Union using the LUCAS Dataset, Remote Sensing, 12, 3479, https://doi.org/10.3390/rs12213479, 2020.

Ghorbanian, A., Kakooei, M., Amani, M., Mahdavi, S., Mohammadzadeh, A., and Hasanlou, M.: Improved land cover map of Iran using Sentinel imagery within Google Earth Engine and a novel automatic workflow for land cover classification using migrated training samples, ISPRS Journal of Photogrammetry and Remote Sensing, 167, 276-288, https://doi.org/10.1016/j.isprsjprs.2020.07.013, 2020.

Giri, C., Pengra, B., Long, J., and Loveland, T. R.: Next generation of global land cover characterization, mapping, and monitoring, International Journal of Applied Earth Observation and Geoinformation, 25, 30-37, https://doi.org/10.1016/j.jag.2013.03.005, 2013.

Gislason, P. O., Benediktsson, J. A., and Sveinsson, J. R.: Random Forests for land cover classification, Pattern Recognition Letters, 27, 294-300, https://doi.org/10.1016/j.patrec.2005.08.011, 2006.

Gong, P., Liu, H., Zhang, M., Li, C., Wang, J., Huang, H., Clinton, N., Ji, L., Li, W., Bai, Y., Chen, B., Xu, B., Zhu, Z., Yuan, C., Ping Suen, H., Guo, J., Xu, N., Li, W., Zhao, Y., Yang, J., Yu, C., Wang, X., Fu, H., Yu, L., Dronova, I., Hui, F., Cheng, X., Shi, X., Xiao, F., Liu, Q., and Song, L.: Stable classification with limited sample: transferring a 30-m resolution sample set collected in 2015 to mapping 10-m resolution global land cover in 2017, Science Bulletin, 64, 370-373, https://doi.org/10.1016/j.scib.2019.03.002, 2019.

Gong, P., Wang, J., and Huang, H.: Stable classification with limited samples in global land cover mapping: Theory and experiments, Science Bulletin, doi: 10.1016/j.scib.2024.03.040, 2024. https://doi.org/10.1016/j.scib.2024.03.040, 2024.

Gong, P., Wang, J., Yu, L., Zhao, Y., Zhao, Y., Liang, L., Niu, Z., Huang, X., Fu, H., Liu, S., Li, C., Li, X., Fu, W., Liu, C., Xu, Y., Wang, X., Cheng, Q., Hu, L., Yao, W., Zhang, H., Zhu, P., Zhao, Z., Zhang, H., Zheng, Y., Ji, L., Zhang, Y., Chen, H., Yan, A., Guo, J., Yu, L., Wang, L., Liu, X., Shi, T., Zhu, M., Chen, Y., Yang, G., Tang, P., Xu, B., Giri, C., Clinton, N., Zhu, Z., Chen, J., and Chen, J.: Finer resolution observation and monitoring of global land cover: first mapping results with Landsat TM and ETM+ data, International Journal of Remote Sensing, 34, 2607-2654, https://doi.org/10.1080/01431161.2012.748992, 2013.

Hansen, M. C., Egorov, A., Potapov, P. V., Stehman, S. V., Tyukavina, A., Turubanova, S. A., Roy, D. P., Goetz, S. J., Loveland, T. R., Ju, J., Kommareddy, A., Kovalskyy, V., Forsyth, C., and Bents, T.: Monitoring conterminous United States (CONUS) land cover change with Web-Enabled Landsat Data (WELD), Remote Sensing of Environment, 140, 466-484, https://doi.org/10.1016/j.rse.2013.08.014, 2014.

Homer, C., Dewitz, J., Jin, S., Xian, G., Costello, C., Danielson, P., Gass, L., Funk, M., Wickham, J., Stehman, S., Auch, R., and Riitters, K.: Conterminous United States land cover change patterns 2001–2016 from the 2016 National Land Cover Database, ISPRS Journal of Photogrammetry and Remote Sensing, 162, 184-199, https://doi.org/10.1016/j.isprsjprs.2020.02.019, 2020.

Huang, X., Song, Y., Yang, J., Wang, W., Ren, H., Dong, M., Feng, Y., Yin, H., and Li, J.: Toward accurate mapping of 30-m time-series global impervious surface area (GISA), International Journal of Applied Earth Observation and Geoinformation, 109, 102787, https://doi.org/10.1016/j.jag.2022.102787, 2022.

Jin, H., Stehman, S. V., and Mountrakis, G.: Assessing the impact of training sample selection on accuracy of an urban classification: a case study in Denver, Colorado, International Journal of Remote Sensing, 35, 2067-2081, https://doi.org/10.1080/01431161.2014.885152, 2014.

Jin, S., Dewitz, J., Li, C., Sorenson, D., Zhu, Z., Shogib, M. R. I., Danielson, P., Granneman, B., Costello, C., Case, A., and Gass, L.: National Land Cover Database 2019: A Comprehensive Strategy for Creating the 1986–2019 Forest Disturbance Product, Journal of Remote Sensing, 3, https://doi.org/10.34133/remotesensing.0021, 2023.

Karra, K., Kontgis, C., Statman-Weil, Z., Mazzariello, J. C., Mathis, M., and Brumby, S. P.: Global land use / land cover with Sentinel 2 and deep learning, doi: 10.1109/igarss47720.2021.9553499, 2021. 4704-4707, https://doi.org/10.1109/igarss47720.2021.9553499, 2021.

779 Li, B., Xu, X., Liu, X., Shi, Q., Zhuang, H., Cai, Y., and He, D.: An improved global land cover mapping in 2015 with
780 30 m resolution (GLC-2015) based on a multisource product-fusion approach, Earth Syst. Sci. Data, 15, 2347-
781 2373, https://doi.org/10.5194/essd-15-2347-2023, 2023.

782 Li, C., Peng, G., Wang, J., Zhu, Z., Biging, G. S., Yuan, C., Hu, T., Zhang, H., Wang, Q., and Li, X.: The first all-season
783 sample set for mapping global land cover with Landsat-8 data, Science Bulletin, 62, 508-515,
784 https://doi.org/10.1016/j.scib.2017.03.011, 2017.

785 Li, C., Wang, J., Wang, L., Hu, L., and Gong, P.: Comparison of Classification Algorithms and Training Sample Sizes in
786 Urban Land Classification with Landsat Thematic Mapper Imagery, Remote Sensing, 6, 964-983,
787 https://doi.org/10.3390/rs6020964, 2014.

788 Li, X., Gong, P., Zhou, Y., Wang, J., Bai, Y., Chen, B., Hu, T., Xiao, Y., Xu, B., Yang, J., Liu, X., Cai, W., Huang, H., Wu,
789 T., Wang, X., Lin, P., Li, X., Chen, J., He, C., Li, X., Yu, L., Clinton, N., and Zhu, Z.: Mapping global urban boundaries
790 from the global artificial impervious area (GAIA) data, Environmental Research Letters, 15, 094044,
791 https://doi.org/10.1088/1748-9326/ab9be3, 2020.

792 Liu, C., Frazier, P., and Kumar, L.: Comparative assessment of the measures of thematic classification accuracy, Remote
793 Sensing of Environment, 107, 606-616, https://doi.org/10.1016/j.rse.2006.10.010, 2007.

794 Liu, L. and Zhang, X.: GLC_FCS10: global 10 m land-cover dataset with fine classification sys tem from Sentinel-1 and
795 2 time-series data, Zenodo [data set]. Liu, L. and Zhang, X. (Eds.), Zenodo, 2025.

796 Liu, L., Zhang, X., Gao, Y., Chen, X., Shuai, X., and Mi, J.: Finer-Resolution Mapping of Global Land Cover: Recent
797 Developments, Consistency Analysis, and Prospects, Journal of Remote Sensing, 2021, 1-38,
798 https://doi.org/10.34133/2021/5289697, 2021.

799 Mao, D., Wang, Z., Du, B., Li, L., Tian, Y., Jia, M., Zeng, Y., Song, K., Jiang, M., and Wang, Y.: National wetland mapping
800 in China: A new product resulting from object-based and hierarchical classification of Landsat 8 OLI images, ISPRS
801 Journal of Photogrammetry and Remote Sensing, 164, 11-25, https://doi.org/10.1016/j.isprsjprs.2020.03.020, 2020.

802 Mellor, A., Boukir, S., Haywood, A., and Jones, S.: Exploring issues of training data imbalance and mislabelling on random
803 forest performance for large area land cover classification using the ensemble margin, ISPRS Journal of Photogrammetry
804 and Remote Sensing, 105, 155-168, https://doi.org/10.1016/j.isprsjprs.2015.03.014, 2015.

805 Morales, C., Díaz, A. S.-P., Dionisio, D., Guarnieri, L., Marchi, G., Maniatis, D., and Mollicone, D.: Earth Map: A Novel
806 Tool for Fast Performance of Advanced Land Monitoring and Climate Assessment, Journal of Remote Sensing, 3,
807 https://doi.org/10.34133/remotesensing.0003, 2023.

808 Nelson, M. D., Garner, J. D., Tavernia, B. G., Stehman, S. V., Riemann, R. I., Lister, A. J., and Perry, C. H.: Assessing map
809 accuracy from a suite of site-specific, non-site specific, and spatial distribution approaches, Remote Sensing of
810 Environment, 260, 112442, https://doi.org/10.1016/j.rse.2021.112442, 2021.

811 Parente, L., Sloat, L., Mesquita, V., Consoli, D., Stanimirova, R., Hengl, T., Bonannella, C., Teles, N., Wheeler, I., Hunter,
812 M., Ehrmann, S., Ferreira, L., Mattos, A. P., Oliveira, B., Meyer, C., Şahin, M., Witjes, M., Fritz, S., Malek, Z., and Stolle,
813 F.: Annual 30-m maps of global grassland class and extent (2000–2022) based on spatiotemporal Machine Learning,
814 Scientific Data, 11, https://doi.org/10.1038/s41597-024-04139-6, 2024.

815 Pelletier, C., Valero, S., Inglada, J., Champion, N., Marais Sicre, C., and Dedieu, G.: Effect of Training Class Label Noise
816 on Classification Performances for Land Cover Mapping with Satellite Image Time Series, Remote Sensing, 9, 173,
817 https://doi.org/10.3390/rs9020173, 2017.

818 Prošek, J. and Šímová, P.: UAV for mapping shrubland vegetation: Does fusion of spectral and vertical information derived
819 from a single sensor increase the classification accuracy?, International Journal of Applied Earth Observation and
820 Geoinformation, 75, 151-162, https://doi.org/10.1016/j.jag.2018.10.009, 2019.

821 Radeloff, V. C., Roy, D. P., Wulder, M. A., Anderson, M., Cook, B., Crawford, C. J., Friedl, M., Gao, F., Gorelick, N.,
822 Hansen, M., Healey, S., Hostert, P., Hulley, G., Huntington, J. L., Johnson, D. M., Neigh, C., Lyapustin, A., Lymburner, L.,

Pahlevan, N., Pekel, J.-F., Scambos, T. A., Schaaf, C., Strobl, P., Woodcock, C. E., Zhang, H. K., and Zhu, Z.: Need and vision for global medium-resolution Landsat and Sentinel-2 data products, Remote Sensing of Environment, 300, 113918, https://doi.org/10.1016/j.rse.2023.113918, 2024.

Radoux, J., Lamarche, C., Van Bogaert, E., Bontemps, S., Brockmann, C., and Defourny, P.: Automated Training Sample Extraction for Global Land Cover Mapping, Remote Sensing, 6, 3965-3987, https://doi.org/10.3390/rs6053965, 2014.

Rodriguez-Galiano, V. F., Chica-Olmo, M., Abarca-Hernandez, F., Atkinson, P. M., and Jeganathan, C.: Random Forest classification of Mediterranean land cover using multi-seasonal imagery and multi-seasonal texture, Remote Sensing of Environment, 121, 93-107, https://doi.org/10.1016/j.rse.2011.12.003, 2012.

Stanimirova, R., Tarrio, K., Turlej, K., McAvoy, K., Stonebrook, S., Hu, K. T., Arevalo, P., Bullock, E. L., Zhang, Y., Woodcock, C. E., Olofsson, P., Zhu, Z., Barber, C. P., Souza, C. M., Jr., Chen, S., Wang, J. A., Mensah, F., Calderon-Loor, M., Hadjikakou, M., Bryan, B. A., Graesser, J., Beyene, D. L., Mutasha, B., Siame, S., Siampale, A., and Friedl, M. A.: A global land cover training dataset from 1984 to 2020, Sci Data, 10, 879, https://doi.org/10.1038/s41597-023-02798-5, 2023.

Stehman, S. V., Olofsson, P., Woodcock, C. E., Herold, M., and Friedl, M. A.: A global land-cover validation data set, II: augmenting a stratified sampling design to estimate accuracy by region and land-cover class, International Journal of Remote Sensing, 33, 6975-6993, https://doi.org/10.1080/01431161.2012.695092, 2012.

Stehman, S. V., Pengra, B. W., Horton, J. A., and Wellington, D. F.: Validation of the U.S. Geological Survey's Land Change Monitoring, Assessment and Projection (LCMAP) Collection 1.0 annual land cover products 1985–2017, Remote Sensing of Environment, 265, 112646, https://doi.org/10.1016/j.rse.2021.112646, 2021.

Sulla-Menashe, D., Gray, J. M., Abercrombie, S. P., and Friedl, M. A.: Hierarchical mapping of annual global land cover 2001 to present: The MODIS Collection 6 Land Cover product, Remote Sensing of Environment, 222, 183-194, https://doi.org/10.1016/j.rse.2018.12.013, 2019.

Sun, L., Yang, T., Lou, Y., Shi, Q., and Zhang, L.: Paddy Rice Mapping Based on Phenology Matching and Cultivation Pattern Analysis Combining Multi-Source Data in Guangdong, China, Journal of Remote Sensing, 4, https://doi.org/10.34133/remotesensing.0152, 2024.

Tachikawa, T., Kaku, M., Iwasaki, A., Gesch, D. B., Oimoen, M. J., Zhang, Z., Danielson, J., Krieger, T., Curtis, B., and Haase, J.: ASTER Global Digital Elevation Model Version 2 – Summary of validation results, Kim Fakultas Sastra Dan Budaya, doi: 10.1093/oxfordjournals.pubmed.a024792, 2011. https://doi.org/10.1093/oxfordjournals.pubmed.a024792, 2011.

Tang, X., Bratley, K. H., Cho, K., Bullock, E. L., Olofsson, P., and Woodcock, C. E.: Near real-time monitoring of tropical forest disturbance by fusion of Landsat, Sentinel-2, and Sentinel-1 data, Remote Sensing of Environment, 294, 113626, https://doi.org/10.1016/j.rse.2023.113626, 2023.

Torres, R., Snoeij, P., Geudtner, D., Bibby, D., Davidson, M., Attema, E., Potin, P., Rommen, B., Floury, N., Brown, M., Traver, I. N., Deghaye, P., Duesmann, B., Rosich, B., Miranda, N., Bruno, C., L'Abbate, M., Croci, R., Pietropaolo, A., Huchler, M., and Rostan, F.: GMES Sentinel-1 mission, Remote Sensing of Environment, 120, 9-24, https://doi.org/10.1016/j.rse.2011.05.028, 2012.

Tsendbazar, N., Herold, M., Li, L., Tarko, A., de Bruin, S., Masiliunas, D., Lesiv, M., Fritz, S., Buchhorn, M., Smets, B., Van De Kerchove, R., and Duerauer, M.: Towards operational validation of annual global land cover maps, Remote Sensing of Environment, 266, 112686, https://doi.org/10.1016/j.rse.2021.112686, 2021.

Wang, Y., Sun, Y., Cao, X., Wang, Y., Zhang, W., and Cheng, X.: A review of regional and Global scale Land Use/Land Cover (LULC) mapping products generated from satellite remote sensing, ISPRS Journal of Photogrammetry and Remote Sensing, 206, 311-334, https://doi.org/10.1016/j.isprsjprs.2023.11.014, 2023.

Wang, Y., Xu, Y., Xu, X., Jiang, X., Mo, Y., Cui, H., Zhu, S., and Wu, H.: Evaluation of six global high-resolution global land cover products over China, International Journal of Digital Earth, 17, https://doi.org/10.1080/17538947.2023.2301673, 2024.

867 Wickham, J., Stehman, S. V., Sorenson, D. G., Gass, L., and Dewitz, J. A.: Thematic accuracy assessment of the NLCD
868 2016 land cover for the conterminous United States, Remote Sensing of Environment, 257, 112357,
869 https://doi.org/10.1016/j.rse.2021.112357, 2021.

870 Wilen, B. O. and Bates, M.: The US fish and wildlife service's national wetlands inventory project. In: Classification and
871 inventory of the world's wetlands, Wilen, B. O. and Bates, M. (Eds.), Springer, 1995.

872 Worthington, T. A., Spalding, M., Landis, E., Maxwell, T. L., Navarro, A., Smart, L. S., and Murray, N. J.: The distribution
873 of global tidal marshes from Earth observation data, Global Ecology and Biogeography, doi: 10.1111/geb.13852, 2024.
874 https://doi.org/10.1111/geb.13852, 2024.

875 Xian, G. Z., Smith, K., Wellington, D., Horton, J., Zhou, Q., Li, C., Auch, R., Brown, J. F., Zhu, Z., and Reker, R. R.:
876 Implementation of the CCDC algorithm to produce the LCMAP Collection 1.0 annual land surface change product, Earth
877 Syst. Sci. Data, 14, 143-162, https://doi.org/10.5194/essd-14-143-2022, 2022.

878 Xie, S., Liu, L., and Yang, J.: Time-Series Model-Adjusted Percentile Features: Improved Percentile Features for Land-
879 Cover Classification Based on Landsat Data, Remote Sensing, 12, 3091, https://doi.org/10.3390/rs12183091, 2020.

880 Xu, F., Shi, Y., Yang, W., Xia, G.-S., and Zhu, X. X.: CloudSeg: A multi-modal learning framework for robust land cover
881 mapping under cloudy conditions, ISPRS Journal of Photogrammetry and Remote Sensing, 214, 21-32,
882 https://doi.org/10.1016/j.isprsjprs.2024.06.001, 2024a.

883 Xu, P., Herold, M., Tsendbazar, N.-E., and Clevers, J. G. P. W.: Towards a comprehensive and consistent global aquatic
884 land cover characterization framework addressing multiple user needs, Remote Sensing of Environment, 250, 112034,
885 https://doi.org/10.1016/j.rse.2020.112034, 2020.

886 Xu, P., Tsendbazar, N.-E., Herold, M., de Bruin, S., Koopmans, M., Birch, T., Carter, S., Fritz, S., Lesiv, M., Mazur, E.,
887 Pickens, A., Potapov, P., Stolle, F., Tyukavina, A., Van De Kerchove, R., and Zanaga, D.: Comparative validation of recent
888 10 m-resolution global land cover maps, Remote Sensing of Environment, 311, 114316,
889 https://doi.org/10.1016/j.rse.2024.114316, 2024b.

890 Yang, J. and Huang, X.: The 30 m annual land cover dataset and its dynamics in China from 1990 to 2019, Earth Syst. Sci.
891 Data, 13, 3907-3925, https://doi.org/10.5194/essd-13-3907-2021, 2021.

892 Yu, L., Wang, J., Li, X., Li, C., Zhao, Y., and Gong, P.: A multi-resolution global land cover dataset through multisource
893 data aggregation, Science China Earth Sciences, 57, 2317-2329, https://doi.org/10.1007/s11430-014-4919-z, 2014.

894 Zanaga, D., Van De Kerchove, R., De Keersmaecker, W., Souverijns, N., Brockmann, C., Quast, R., Wevers, J., Grosu, A.,
895 Paccini, A., and Vergnaud, S.: ESA WorldCover 10 m 2020 v100, Zenodo: Geneve, Switzerland, doi:
896 10.5281/zenodo.5571936, 2021. https://doi.org/10.5281/zenodo.5571936, 2021.

897 Zhang, H. K. and Roy, D. P.: Using the 500 m MODIS land cover product to derive a consistent continental scale 30 m
898 Landsat land cover classification, Remote Sensing of Environment, 197, 15-34, https://doi.org/10.1016/j.rse.2017.05.024,
899 2017.

900 Zhang, X., Liu, L., Chen, X., Gao, Y., Xie, S., and Mi, J.: GLC_FCS30: global land-cover product with fine classification
901 system at 30 m using time-series Landsat imagery, Earth Syst. Sci. Data, 13, 2753-2776, https://doi.org/10.5194/essd-13-
902 2753-2021, 2021.

903 Zhang, X., Liu, L., Chen, X., Xie, S., and Gao, Y.: Fine Land-Cover Mapping in China Using Landsat Datacube and an
904 Operational SPECLib-Based Approach, Remote Sensing, 11, 1056, https://doi.org/10.3390/rs11091056, 2019.

905 Zhang, X., Liu, L., Wang, J., Zhao, T., Liu, W., and Chen, X.: Automated Mapping of Global 30-m Tidal Flats Using Time-
906 Series Landsat Imagery: Algorithm and Products, Journal of Remote Sensing, 3,
907 https://doi.org/10.34133/remotesensing.0091, 2023a.

908 Zhang, X., Liu, L., Wu, C., Chen, X., Gao, Y., Xie, S., and Zhang, B.: Development of a global 30 m impervious surface
909 map using multisource and multitemporal remote sensing datasets with the Google Earth Engine platform, Earth Syst. Sci.
910 Data, 12, 1625-1648, https://doi.org/10.5194/essd-12-1625-2020, 2020.

911 Zhang, X., Liu, L., Zhang, W., Guan, L., Bai, M., Zhao, T., Zhehua, L., and Chen, X.: Tracking gain and loss of impervious
912 surfaces by integrating continuous change detection and multitemporal classifications from 1985 to 2022 in Beijing,
913 International Journal of Applied Earth Observation and Geoinformation, 135, 104268,
914 https://doi.org/10.1016/j.jag.2024.104268, 2024a.

915 Zhang, X., Liu, L., Zhao, T., Chen, X., Lin, S., Wang, J., Mi, J., and Liu, W.: GWL_FCS30: a global 30 m wetland map
916 with a fine classification system using multi-sourced and time-series remote sensing imagery in 2020, Earth Syst. Sci. Data,
917 15, 265-293, https://doi.org/10.5194/essd-15-265-2023, 2023b.

918 Zhang, X., Liu, L., Zhao, T., Gao, Y., Chen, X., and Mi, J.: GISD30: global 30 m impervious-surface dynamic dataset from
919 1985 to 2020 using time-series Landsat imagery on the Google Earth Engine platform, Earth Syst. Sci. Data, 14, 1831-
920 1856, https://doi.org/10.5194/essd-14-1831-2022, 2022.

921 Zhang, X., Liu, L., Zhao, T., Wang, J., Liu, W., and Chen, X.: Global annual wetland dataset at 30 m with a fine
922 classification system from 2000 to 2022, Scientific Data, 11, https://doi.org/10.1038/s41597-024-03143-0, 2024b.

923 Zhang, X., Zhao, T., Xu, H., Liu, W., Wang, J., Chen, X., and Liu, L.: GLC_FCS30D: the first global 30 m land-cover
924 dynamics monitoring product with a fine classification system for the period from 1985 to 2022 generated using dense-
925 time-series Landsat imagery and the continuous change-detection method, Earth Syst. Sci. Data, 16, 1353-1381,
926 https://doi.org/10.5194/essd-16-1353-2024, 2024c.

927 Zhao, T., Zhang, X., Gao, Y., Mi, J., Liu, W., Wang, J., Jiang, M., and Liu, L.: Assessing the Accuracy and Consistency of
928 Six Fine-Resolution Global Land Cover Products Using a Novel Stratified Random Sampling Validation Dataset, Remote
929 Sensing, 15, 2285, https://doi.org/10.3390/rs15092285, 2023.

930 Zhu, Z., Gallant, A. L., Woodcock, C. E., Pengra, B., Olofsson, P., Loveland, T. R., Jin, S., Dahal, D., Yang, L., and Auch,
931 R. F.: Optimizing selection of training and auxiliary data for operational land cover classification for the LCMAP initiative,
932 ISPRS Journal of Photogrammetry and Remote Sensing, 122, 206-221, https://doi.org/10.1016/j.isprsjprs.2016.11.004,
933 2016.

934